이학박사 학위논문

Spin dynamics under spin Hall effect modulation: Skyrmion oscillator

스핀 홀 효과 조정영역에서의 스핀 동역학: 스커미온 진동자

2019년 08월

서울대학교 대학원

물리천문학부

황 현 석

Spin dynamics under spin Hall effect modulation: Skyrmion oscillator

스핀 홀 효과 조정영역에서의 스핀 동역학: 스커미온 진동자

지도교수 최석봉

이 논문을 이학박사 학위논문으로 제출함

2019년 08월

서울대학교 대학원
물리천문학부
황 현 석

황현석의 이학박사 학위논문을 인준함

2019년 06월

위 원 장 김 창 영 (인)

부위원장 최 석 봉 (인)

위 원 박 철 환 (인)

위 원 이 진 호 (인)

위 원 김 동 현 (인)

Spin dynamics under spin Hall effect modulation: Skyrmion oscillator

Hyun-Seok Whang

Supervised by
Professor Sug-Bong Choe

A Dissertation in Physics

Submitted to the Faculties of
Seoul National University
in Partial Fulfillment of the Requirements for the Degree of
Doctor of Philosophy

July 2019

Department of Physics and Astronomy
The Graduate College of Natural Sciences
Seoul National University

Abstract

A magnet exhibits semi-permanent magnetic field, unless the ordering of magnetic moments does not break by external factors. This so-called non-volatility of magnetization can be harnessed to realize a power-efficient data storage, provided with proper mechanisms to modify the magnetization. These mechanisms were established by the discovery of giant magnetoresistance and spin-polarized current in the 1980s, which enabled the electric detection and control of magnetization, respectively. The concept of spin finally entered the field of electronics, which consecutively led to successful applications in the logic and memory devices. This associated field of study is called the spintronics, also known as the spin electronics.

Since the spintronics is involved deeply with the collective ordering of the spins, the constraints bestowed upon the system not only expand the phenomena toward exotic dynamics but also provide design rules to achieve desirable properties. Among various possible constraints, a simple tri-layered system of a ferromagnetic thin film sandwiched between two nonmagnetic layers, exhibit surprisingly complex spin dynamics depending on the choice of the materials and their respective thicknesses. As a result, the current-induced spin dynamics in this tri-layered magnetic system is mainly studied throughout the thesis.

Amid the various interesting dynamics of a tri-layered film, the spin-Hall effect (SHE) in the sandwiching heavy metal layers that transfer spin polarized current into the ferromagnetic layer, stands out

with its design capabilities. Since the magnitude and sign of the spin polarized current by SHE depends on the material and its thickness, one can manipulate the transferred spin torque by modulating the thickness of the sandwiching layers. This technique is called the spin-Hall-effect modulation and exhibits some interesting features. The thesis is mainly directed on searching what and how exotic spin dynamics happen at the wires with laterally modulated SHE, via micromagnetic simulations and analytic equation analysis.

Chapter 2 shows how the current-driven domain wall (DW) pins and depins from various types of spin-Hall-effect-modulation boundaries. The method of unidirectional depinning from given modulation boundaries are investigated. This unidirectional depinning behavior provides a systematic mechanism to precisely move a DW step-by-step toward next modulation boundaries only by alternating the direction of electric current, which will assist the realization of a racetrack memory.

Chapter 3 is the highlight of this study where we propose a whole new concept of spin-torque oscillator, based on magnetic skyrmion dynamics subject to lateral modulation of the SHE. In the oscillator, a skyrmion circulates around the modulation boundary between opposite SHE-torque regions, where the SHE pushes the skyrmion in the opposite direction, toward the modulation boundary. A micromagnetic simulation confirms such oscillations. This SHE-modulation-based skyrmion oscillator is expected to overcome the troubling issues of conventional spin-torque oscillators.

As part of recent approaches to search for possible applications of spintronic devices, neuromorphic engineering is also briefly discussed in Chapter 4. A neuron device with integrate-and-fire feature is realized via current-driven DW motion in a wire with a magnetic tunnel junction at the end. With the already proposed idea of a DW synapse device, all-DW-based artificial neural network can be realized.

Additionally, miscellaneous analytic equations were derived to help magnetic-parameter measurement and to offer design rules for certain properties. The depinning current from a triangle notch, the equations to measure spin-orbit torque at any initial angle and the equations to measure anisotropy field from magneto optical Kerr effect setup are derived from associated analytic models and explained in Chapter 5.

Findings analyzed in this thesis provide the latest understanding of the spin-Hall effect modulated systems and some others. The explained spin dynamics in these systems not only exhibit properties that can better the state-of-the-art applications, but also triggers new possibilities to design in completely unconventional ways.

Keywords: domain wall, current-induced domain wall motion, skyrmion, spin-Hall effect, spin-Hall-effect modulation, ferrimagnetic systems, skyrmion, spin-torque oscillator, neuromorphic engineering.

Student number: 2013-22999

Contents

List of Figures

Chapter 1. Introduction

The story of the magnetism dates its origin all the way back to naturally magnetized lodestones described by Thales of Miletus 2,500 years ago. It was not until 12th century that magnets were utilized technically as compasses for navigation. The understanding of the phenomena started in 1819 with the discovery of the relationship between electricity and magnetism by Hans Christian Ørsted. The electromagnetism formulated by James Clerk Maxwell became one of the most important scientific milestones in human history. Following the rapid growth of electromagnetic devices and computer technology, the discovery of giant magnetoresistance [1] and spin-polarized current [2-6] in the 1980s, further pushed the possibilities of electromagnetism into the field of spintronics where one can control and detect spins electrically.

With the global need to realize smaller, faster and low-power logic and memory devices especially for the so-called 4th industrial revolution, the spintronics has also developed accordingly. From bulk ferromagnetic materials into ferromagnetic thin films, from in-plane magnetic anisotropy to perpendicular magnetic anisotropy (PMA), from field-driven motion to current-driven motion, from spin-transfer torque (STT) to spin-orbit torque (SOT), and finally into Dzyaloshinskii-Moriya interaction (DMI), skyrmions, ferrimagnetic systems and more to date, spintronics expanded into various systems.

It is notable here that these systems and exotic dynamics within is defined by the constraints. Among various constraints possible, the

interfaces between ferromagnetic thin film and its sandwiching layers play a crucial role determining the inherent properties such as the magnetic anisotropy, spin-orbit torque, Dzyaloshinskii-Moriya interaction and so on. As the constraints break the symmetries of the system, a new dynamics arise that can be harvested into new device applications.

This thesis focuses on what and how the spin dynamics change for different set of controlled constraints. This chapter clarifies the ingredients necessary to understand the dynamics under those constraints. As mentioned previously, following the history of developing spintronics, magnetic anisotropy, spin torque, skyrmions and ferrimagnets are explained accordingly with necessary details in between. Finally, the micromagnetic simulation which is the main methodology for the thesis is briefly explained.

1.1 Magnetic anisotropy

The bulk ferromagnetic material aligns the spin with its neighbors via exchange coupling that results in domains with same magnetization direction. This is called the ferromagnetic ordering. The domain's magnetization direction is affected inherently by the atomic structure through spin orbit interaction and externally by the total shape of the material through demagnetizing field. The preference of magnetization direction toward certain axis is called the magnetic anisotropy.

For a ferromagnetic thin film, the magnetization tends to align along the film plane due to the shape anisotropy induced by the demagnetizing field. This is called the in-plane magnetic anisotropy (IMA). However, if the thin film is attached to another layer, the interaction along the interface can align the magnetization in the film normal axis. This is called the perpendicular magnetic anisotropy (PMA). Figure 1.1 illustrates the domains in IMA and PMA films respectively.

The PMA holds a great feature in digital application since the domain is restricted to up/down state which respectively corresponds to the 1 and 0 in digital memory. Since the domain and its boundary, domain wall (DW) can be manipulated by the external magnetic field and injected current, the DW dynamics in ferromagnetic thin film with the PMA holds some great possibilities as a candidate of logic and memory devices.

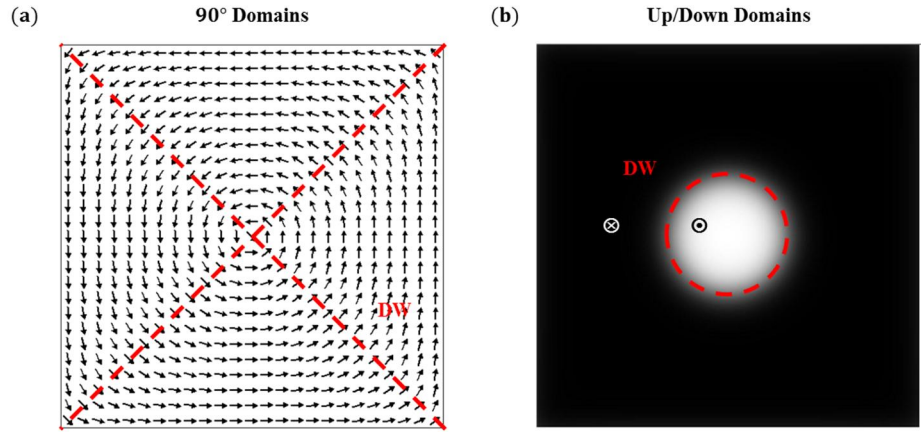

Figure 1.1 Domains and DW in ferromagnetic thin films with **a**, IMA **b**, PMA. The red dotted line is the boundary between domains called the domain wall (DW). The magnetization is represented as a, arrow and b, the greyscale color gradient (magnitude of the film normal component of magnetization).

1.2 Spin torque

Since the conducting electron's spin interacts with the local magnetization of the ferromagnetic material, magnetization experiences torque under the injection of electric current. This spin torque is the essential mechanism that enables the electric control of the magnetization.

1.2.1 Spin transfer torque

The conducting electron's spin and local magnetization tends to align to each other and therefore the electron passing through a magnetic domain eventually aligns to the domain's magnetization direction. Hence the electron flow through a thick magnetized domain is polarized in one direction which results in the spin-polarized current.

The same happens for the local magnetization. Under the injection of spin-polarized current, the local magnetization experiences spin torque that rotates the magnetization into the direction of the spin polarization. Eventually, if enough spin-polarized current pass through a magnetic domain, the local magnetization aligns to the spin polarization unless there is some anisotropy forbidding the direction.

This torque directing the interaction between the conduction electron's spin and the local magnetization is called the spin-transfer torque (STT). Electric dynamics of a magnetic domain based on this torque and the resulting current-induced-domain-wall motion (CIDWM) is being studied extensively.

In a one-dimensional DW scheme, the electron passing through a DW rotates to align with the local magnetization site-by-site. Due to the angular momentum conservation, the local magnetization of the domain wall also rotates conversely which effectively moves the DW to the direction of electron flow as illustrated in Fig. 1.2. In conclusion, the DW position can be controlled by spin-transfer torque.

The mechanism illustrated in Fig. 1.2 assumes that the conduction electron adiabatically follows the local magnetization. This is called the adiabatic STT [7-10]. However, this is not always true as in the case of a narrow DW where the local magnetization changes drastically so that the conduction electron cannot follow the change adiabatically [11,12]. This non-adiabatic dynamic is hard to keep track of since the interaction is susceptible to diverse variables. Nevertheless,

it is possible to state all possible torques that comes with 2 degree of freedom as described in the modified Landau-Lifshitz-Gilbert (LLG) Eq. 1.1 [7].

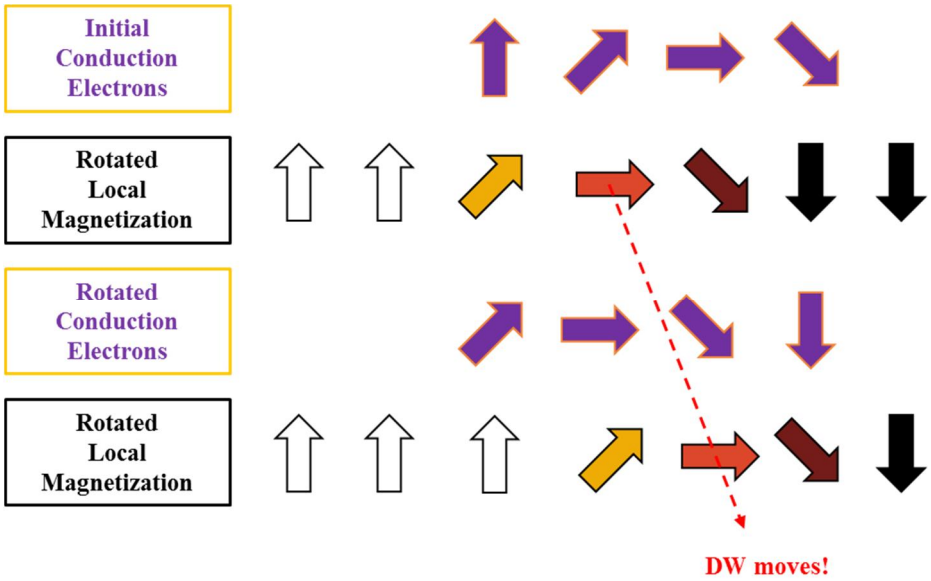

Figure 1.2 Domain wall motion via adiabatic spin-transfer torque. The arrows represent the spin and local magnetization's direction. The red dotted line shows the motion of a DW center.

$$\frac{\mathrm{d}\hat{m}}{\mathrm{d}t} = -\gamma_0 \hat{m} \times \vec{H}_{\mathrm{eff}} + \alpha \hat{m} \times \frac{\mathrm{d}\hat{m}}{\mathrm{d}t} - b_{\mathrm{J}} \hat{m} \times \left(\hat{m} \times \frac{\partial \hat{m}}{\partial x} \right) - c_{\mathrm{J}} \hat{m} \times \frac{\partial \hat{m}}{\partial x} \quad (1.1)$$

The first two terms are respectively the precession and dissipation terms. The third and fourth terms are respectively the adiabatic STT and non-adiabatic STT term. Since these STT terms can describe all possible direction and magnitude of a spin torque, the coefficients b_{J} and c_{J} fully describes how the STT acts on a system.

Although the STT certainly provides a way to manipulate magnetic domains and DWs, due to the precessional effect, the CIDWM induced by STT suffers from Walker breakdown [13] which limits the

speed of the CIDWM. Additionally, the STT mechanism cannot explain the CIDWM along the current direction [14-17] opposite to the electron flow. In addition, various experiments proved the existence of another spin torque other than the STT.

1.2.2 Spin-orbit torque

In a ferromagnetic thin film (FM) sandwiched between nonmagnetic heavy metal (HM) layers where the structure was originally established to obtain PMA, the spin-orbit-coupling-related phenomena at the interfaces and in HMs also bring about a new spin torque. One of the phenomena is the spin-Hall effect (SHE) [18-20] from HM and the Rashba effect [21-25] at the HM/FM interface that is illustrated in Fig. 1.3.

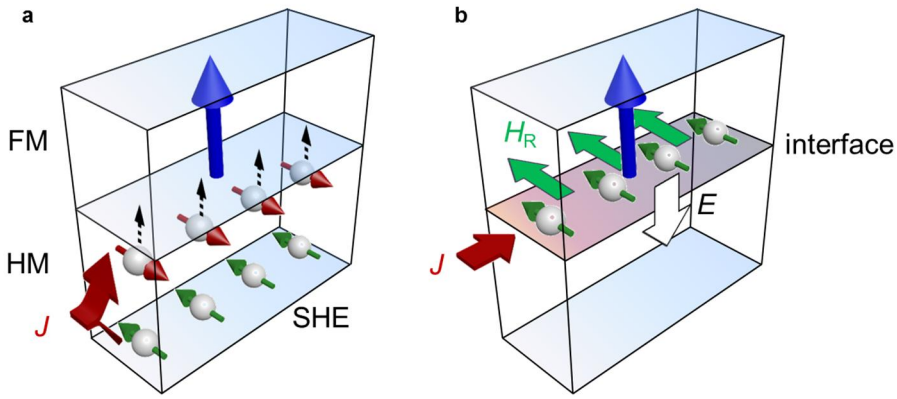

Figure 1.3 Schematics of a spin torque induced by **a**, SHE and **b**, Rashba effect. The red arrow indicates the current flow J, the arrow piercing a small sphere indicates the conduction electron's spin direction. The green arrow shows the direction of the Rashba field, H_R. The blue arrow indicates the injected spin-polarized current.

The spin-orbit coupling in the HM layer generates a spin-polarized current via SHE where the certain direction of spin is

exclusively scattered into the FM layer. On the other hand, the Rashba effect arises from the structural inversion asymmetry (SIA) that results in electric field (Rashba field) that consequently rotates the spin of the electrons scattered into the FM layer. Both models induce spin-polarized current into the FM layer and the spin torque induced by it is named the spin-orbit torque (SOT).

Although the origin of the SOT is still in debate, alike the STT, the induced spin-torque can be described entirely by the modified LLG Eq. 1.2.

$$\frac{\mathrm{d}\hat{m}}{\mathrm{d}t} = -\gamma_0 \hat{m} \times \vec{H}_{\mathrm{eff}} + \alpha \hat{m} \times \frac{\mathrm{d}\hat{m}}{\mathrm{d}t} - \beta_{\mathrm{L}} \hat{m} \times \left(\hat{m} \times \hat{m}_p\right) - \beta_{\mathrm{T}} \hat{m} \times \hat{m}_p \quad (1.2)$$

The equation is basically same with the STT case concept wise, only with the spin-polarization direction injected into FM via SHE and Rashba effect, $\hat{m}_p$ replacing the $\frac{\partial \hat{m}}{\partial x}$. It is notable that the longitudinal term β_{L} directly drives the DW, whereas the transverse term β_T does not. It should also be noted that the SOT only moves a Néel DW which will be discussed in detail later in the magnetic structures chapter.

The SOT is free from Walker breakdown unlike the STT, and generally induces faster DW motion than the STT. This thesis therefore focuses more on the details of SOT rather than STT. In addition, since the SOT from Rashba scheme is harder to manipulate due to its interfacial origin, we focus more on the SHE scheme that is much more generous to possible design options.

1.2.3 Spin-Hall effect modulation

The SHE in the sandwiching HM layers induces spin-polarized current into the FM layer. The spin-Hall coefficient (spin-Hall angle) that determines the magnitude and sign of the spin-polarized current differs from material to material. Furthermore, the thickness of a HM layer determines the magnitude of the spin-polarized current since the amount of scattered, spin-polarized conduction electron into the FM increases with the thickness [26,27]. Therefore, it is possible to manipulate the sign and magnitude of the net spin-polarized current injected by choosing the right materials for HMs and tuning the thicknesses of them. Since the thicknesses of the top and bottom HM layers can be easily modulated, one can ideally fabricate any structures with spatially varying SOT as illustrated in Fig. 1.4. From now on, this technique will be called the

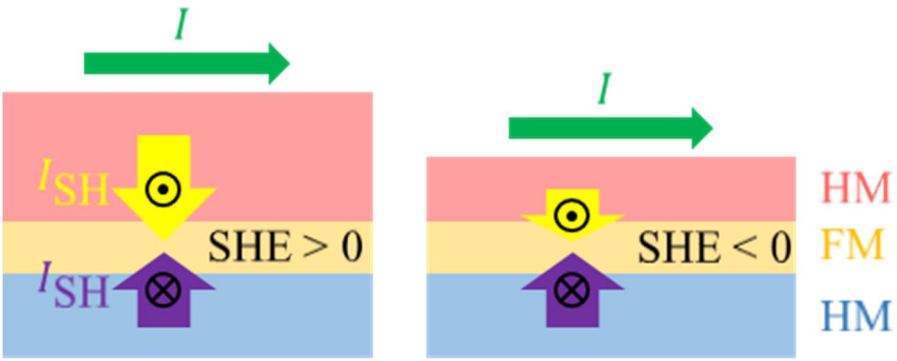

Figure 1.4 Schematics of the SHE-modulation technique. Cross–sectional view of layered structure with SHE modulation. The red, yellow, and blue areas indicate the top HM, FM, and bottom HM layers, respectively. The green arrows show the direction of the electric current, I. The yellow and purple arrows are the directions of spin-polarized current from the top and bottom HM layers, respectively.

SHE-modulation technique and will be the main ingredient of the thesis highlight.

1.3 Magnetic structures

These spin torques generated by the electric current acts on the magnetic structures that eventually results in various spin dynamics. The magnetic structures subject to these spin torques are energy-minima states determined by static energy terms of the system. As already discussed frequently, in a ferromagnetic thin film with PMA, the up/down domains and its boundary, DW is the most common energy-minimum state.

1.3.1 Domain wall

The magnetization is subject to exchange energy, anisotropy energy and magnetostatic energy (demagnetization energy). Since a DW inherently increases the exchange energy and anisotropy energy, DW is not preferred in this scheme. However, since the magnetostatic energy prefers randomized magnetization where the net magnetization is zero, DW is favored in magnetostatic-energy scheme. This competition among the energy terms decides the energy-minimum state with specific domain size and DW length.

In an ideal sample, the manipulated magnetic domains will try to go back to its energy minima whenever the external force is gone.

However, thanks to the exchange energy that restricts the generation of a DW and the pinning sites that hinders the DW motion via small energy barriers across the sample, the DW tends to stay still unless enough external magnetic field or spin torque is present. This makes the DW position non-volatile and consequently, understanding the motion of given initial DWs can conveniently define the entire spin dynamics of the system.

Now since the DW is established into a stable magnetic structure that can represent the whole spin dynamics, the DW type becomes crucial. There are two degree of freedom when it comes to the configuration of a DW. These two types of DW are the Néel wall and the Bloch wall, whose patterns are described in Fig. 1.5.

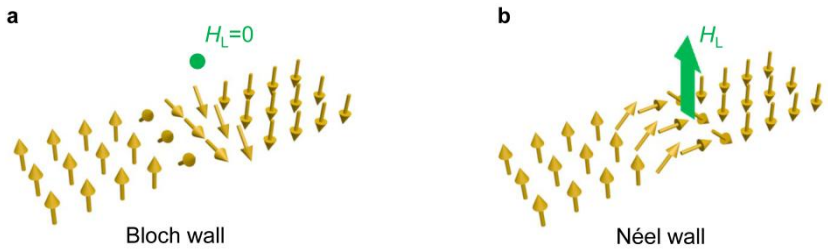

Figure 1.5 Schematics of the DW orientations. a, Bloch wall and **b**, Néel wall and the longitudinal SOT fields (H_L, green) acting on them are illustrated. The yellow arrows represent the magnetization directions.

Although it seems that there are no preferences in the direction a DW rotates, since the DW width (size measured along the direction of change) is usually much smaller than the DW length (size measured perpendicular to the measuring direction of the DW with in the film plane), the magnetostatic energy tends to prefer the Bloch wall

orientation. A rather troubling problem arises here since for a Bloch wall, the longitudinal SOT field is zero, which means that SOT cannot drive the Bloch wall. The Néel wall orientation is necessary for SOT-driven domain wall motion.

1.3.2 Dzyaloshinskii-Moriya interaction

For a Néel wall to be the stable energy-minima orientation of a DW, there needs to be another energy term that prefers the orientation (chirality) of a Néel wall. The search for this puzzle piece led to the introduction of an interfacial Dzyaloshinskii-Moriya interaction (iDMI, DMI) [28]. Due to the broken inversion symmetry (impurities) at the FM/HM interface (Fig. 1.6), the anti-symmetric energy term arises from the spin-orbit coupling that is given by Eq. 1.3 [29-31].

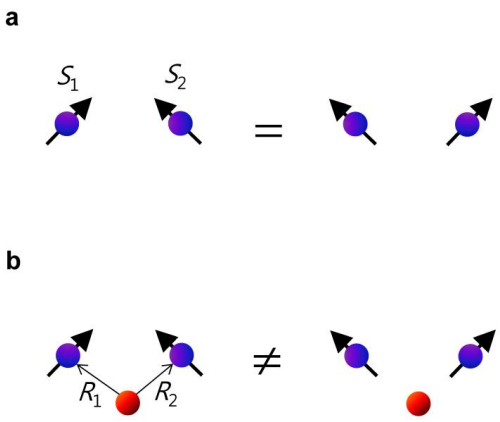

Figure 1.6 Schematics of a, Heisenberg exchange interaction and b, Dzyaloshinskii-Moriya interaction. The arrow piercing purple sphere represents the local magnetization ($S_{1,2}$). The red sphere represents an impurity. The displacement vectors from an impurity to magnetization are shown as arrows with $R_{1,2}$.

$$E_{\mathrm{DMI}} \propto \vec{D} \cdot (\vec{S}_1 \times \vec{S}_2) \quad (1.3)$$

Here, the $\vec{S}$ denotes the local magnetization direction and $\vec{D}$ is the Dzyaloshinskii vector parallel to $\vec{R}_1 \times \vec{R}_2$. Due to this E_{DMI}, the magnetization tends to rotate in a certain fixed chirality that eventually results in a Néel wall orientation. By taking $-\nabla E_{\mathrm{DMI}}$, we find that the DMI-induced effective field $\vec{H}_{\mathrm{DMI}}$ is directed to the magnetization direction of a Néel wall. Since the $\vec{H}_{\mathrm{DMI}}$ can be either positive or negative, there are also positive/negative Néel walls that eventually decides the direction of the SOT-induced DW motion. It is notable that since the direction of a DW motion is determined by the signs of the SOT and the DMI, the DW can move both parallel and antiparallel to the electric current direction unlike the case of adiabatic STT. The SOT and DMI was the right puzzle piece for the mysterious CIDWM from a sandwiched ferromagnetic layer.

1.3.3 Skyrmion

The DMI was first studied extensively due to the promising features of the SOT-induced DW motion enabled by it. Surprisingly, the ripples that the discovery of the DMI caused to the field was not limited to it. Soon it was introduced that a topologically protected magnetic pseudo particle named skyrmion can be realized via DMI [32-38].

Since the DMI preserves the chirality, a shrinking bubble (circular) domain with Néel wall configuration confronts an energy barrier that prohibits the complete annihilation of the domain at certain

domain size. Since the chiral spin structure (Fig. 1.6) has to overcome the DMI energy to disappear, the structure is protected against external energy fluctuations, which eventually makes the structure very stable.

Since the DMI energy preserves the topology of this chiral structure, the skyrmion is said to be topologically protected. Due to this inherent stability and a small particle-like structure, many fresh ideas utilizing the skyrmion as the next candidate of logic and memory devices poured out from the field. The main highlight of this thesis is also based on the dynamics of a skyrmion in a SHE-modulation structure.

Figure 1.7 Schematics of a Néel skyrmion structure.

1.4 Ferrimagnetism

As can be found in LLG equations in Eq. 1.1 and 1.2, the magnetization under spin torque always experiences precession. However, most precession-based phenomena such as the Walker breakdown, DW tilting, skyrmion Hall effect and so on usually tend to hinder the desired motion. Most importantly, the precession-related behaviors increase the net time spent on driving the magnetic structure

into the desired state. For a spintronic device whose operation speed decides its fate, the speed and efficiency lost to precession-based phenomena is a waste. Among the efforts to detour this, it was shown that the antiferromagnetic material exhibits ultrafast DW speed [39] and the system is being studied extensively since. Since the precessional torques of opposite spins with antiferromagnetic coupling cancels each other out, the precessional behavior does not affect the dynamics in antiferromagnetic systems. Consequently, the spin dynamics in antiferromagnetic material are much faster than that of ferromagnets.

However, since the magnetization also cancels out for the antiferromagnetic material, the detection of the magnetization is troublesome. This can be solved via ferrimagnetic material/structure (Fig. 1.8), whose angular momentum compensation point differs from the magnetization compensation point [39-41]. Due to the antiferromagnetic coupling between 2 materials in the ferrimagnetic system, the magnetizations tend to align anti-parallel to each other. As the temperature changes the relative saturation magnetization of respective materials, the net magnetization cancels out to zero ($M_{S1}t_1 = M_{S2}t_2$, $M_{S1,2}$ and $t_{1,2}$ are the saturation magnetizations and thicknesses of the respective layers) at the magnetization compensation point and the net angular momentum cancels out to zero ($M_{S1}t_1/\gamma_1 = M_{S2}t_2/\gamma_2$, $\gamma_{1,2}$ are the gyromagnetic ratios of the respective layers) at the angular momentum compensation point. Since the precessional behaviors are prohibited at the angular momentum compensation point that is different from the magnetization compensation point, the ultrafast dynamics at the

angular momentum compensation point can be detected. This ultrafast dynamic in the ferrimagnetic system is utilized in the chapter 3 to increase the operation frequency of a skyrmion oscillator.

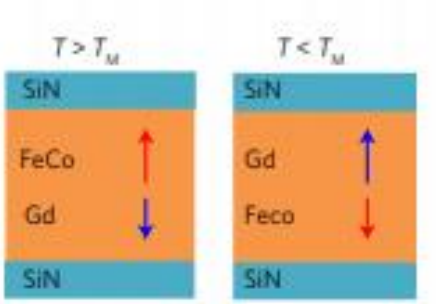

Figure 1.8 Schematics of a synthetic ferrimagnetic structure. The red and blue arrows represent the magnetization of FeCo and Gd layers (orange). The cyan layer is the SiN capping layers. The left and right structure shows the cases of temperature under/over the magnetization compensation temperature T_{M}.

1.5 Micromagnetic simulation

All the ingredients regarding the magnetic structures and their driving torques have now been explained briefly with the exception of the method to study them. In this thesis, the micromagnetic simulation is utilized as the main tool to analyze given systems and verify possible application ideas. Since the micromagnetic simulation excels at predicting the dynamics of a given system, it is a great tool to establish the initiative insight for systems that are yet troublesome to manufacture and too complex to be described with simple analytic models.

The micromagnetic simulation is mostly composed of 4 main

parts as illustrated in the Fig. 1.9. First the geometry of the magnetic region is broken down into regular meshes of unit magnetizations, which becomes the basic stage of the simulation. This mesh is then assigned with the energy terms such as the exchange energy, anisotropy energy, demagnetization energy (magnetostatic energy) and DMI energy. Additionally, the external torque terms induced by the magnetic field and the spin torques (STT and SOT) are applied to the mesh. Finally, this mesh of magnetization is set to evolve accordingly with either the LLG evolver or the minimization evolver. The LLG evolver calculates the magnetization change for each small time steps with the LLG equation to eventually attain the spin dynamics whereas the minimization evolver ignores the time and effectively finds the energy-minimum state.

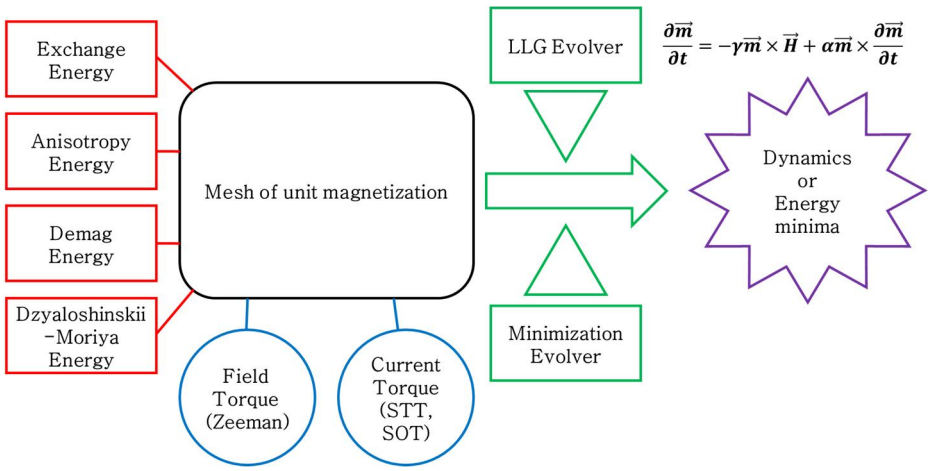

Figure 1.9 Schematics of the micromagnetic simulation.

Provided that proper assumptions are kept in mind, the result of micromagnetic simulation can precisely predict the dynamics of a given system. Consequently, the micromagnetic simulation can provide the clues on how the underlying mechanism works or how the suggested

systems will behave. The former can help the understanding of the real physical system, while the latter can help establishing valid ideas that can improve certain applications.

The object oriented micromagnetic framework (OOMMF) was utilized in all the results in this thesis [42]. The specific details will follow from here on.

Chapter 2. Domain wall pinning/depinning at the spin-Hall-effect modulation boundary

To realize the DW-based logic and memory devices, the position and the motion of a DW should be controlled precisely. This is usually troublesome due to the differing systematic and non-systematic inaccuracies. Commonly, the pinning/depinning behavior of a DW from a geometric notch is utilized to precisely stop the DW at desired positions. However, the technique also suffers from other issues regarding the increasing resistance, inconsistent pinning power, limitations to the driving current and so on. This chapter introduces the spin-Hall-effect-modulation boundary as a new reliable pinning/depinning mechanism that can control the DW positions systematically only by alternating the current direction.

2.1 Introduction

The discovery of CIDWM introduced the idea of a memory device that utilizes the sequence of domains as data packet and by shifting these domains, reads the data packet without any mechanical units as illustrated in Fig. 2.1 [43]. Since the DWs should keep their distances to prevent data deformation, the DW position after the motion should be controlled accurately. The accuracy will eventually limit the storage density. However, due to the inherent random pinning sites, demagnetizing field, DW inertia, precessional DW tilting in SOT induced DW motion, and etc., the position of a DW cannot be easily defined without an additional mechanism to pin a DW at certain position. By introducing multiple pinning sites and utilizing the successive pinning, depinning, motion and pinning cycle through these pinning sites, one can successfully discretize the DW motion.

The most common systematic way to pin a DW is carving a geometrical notch on a wire. Since the DW tends to be the shortest possible to minimize the DW energy that is proportional to its length, DW pins at the bottleneck. This will be discussed in detail later in chapter 5.1. Nevertheless, the notch method suffers from increase in the wire resistance and the limitation on the driving current by the threshold depinning current. Here we provide a new pinning/depinning mechanism that can pin/depin the DWs from a spin-Hall-effect-modulation boundary just by alternating between positive and negative electric current.

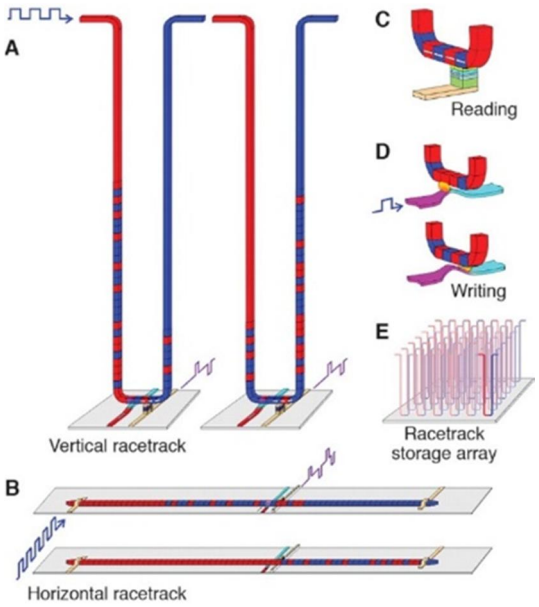

Figure 2.1 Schematics of a racetrack memory (from ref. [43]). a, U-shaped vertical-configuration racetracks. The two cartoons show the magnetic patterns in the racetrack before and after the DWs have moved down one branch, past the read and write elements, and then up the other branch. **b,** Horizontal configurations. **c,** Reading data from the stored pattern is done by measuring the tunnel magnetoresistance of a magnetic tunnel junction element connected to the racetrack. **d,** Writing data is accomplished by the fringing fields of a DW moved in a second ferromagnetic nanowire oriented at right angles to the storage nanowire. **e,** Arrays of racetracks are built on a chip to enable high-density storage.

2.2 Pinning at the spin-Hall-effect-modulation boundary

As explained in the chapter 1.2.3, the sign and magnitude of the SOT can be manipulated by modulating the SHE through the thicknesses of sandwiching layers as shown in Fig. 1.4. Since the sign of the SOT

can be reversed just by changing the thickness of the top layer, one can easily manufacture the spin-Hall-effect-modulation boundary where the sign of the SHE changes across the boundary (Fig. 2.2).

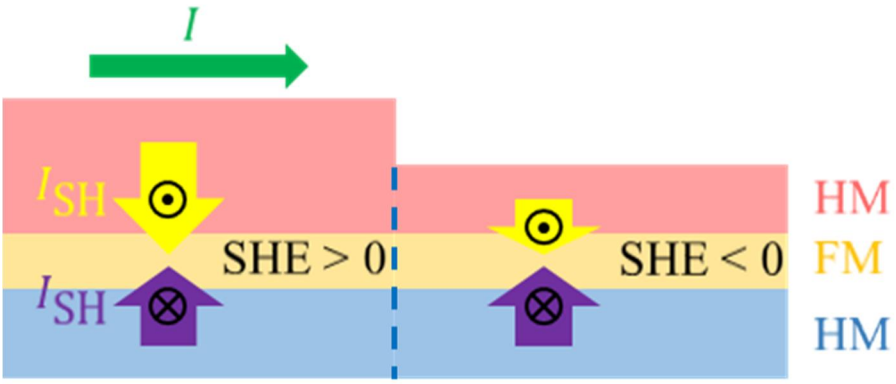

Figure 2.2 Schematics of the spin-Hall-effect-modulation boundary. Cross–sectional view of layered structure with SHE modulation. The red, yellow, and blue areas indicate the top HM, FM, and bottom HM layers, respectively. The green arrow shows the direction of the electric current, I. The yellow and purple arrows are the directions of spin-polarized current from the top and bottom HM layers, respectively. The blue vertical dotted line indicates the spin-Hall-effect-modulation boundary.

Since the magnetic layer and its interfaces are continuous across the SHE-modulation boundary, the magnetic structure and its inherent energies remain consistent. Only the sign of the external SOT by SHE changes across the SHE-modulation boundary. Therefore, for positive current that drives the DW toward the SHE-modulation boundary (positive (negative) current is defined from here on as the direction that drives a DW toward (away from) the SHE-modulation boundary), the DW should always stop at the SHE-modulation boundary. This means that the SHE-modulation boundary works as a perfect pinning site that a DW cannot pass through under any magnitude of applied current. No

matter where the DW starts, since the DW is driven toward the SHE-modulation boundary, DW eventually pins at the spin-Hall-effect-modulation boundary.

2.3 Unstable depinning at the spin-Hall-effect-modulation boundary

With applied positive electric current, the DW always stops at the SHE–modulation boundary (this will be denoted simply as the modulation boundary from now on). Theoretically, the depinning current (threshold current necessary to depin the DW) from the modulation boundary is infinite for positive electric current. One can only depin the DW from the modulation boundary by applying the negative electric current that drives a DW away from the modulation boundary. Flipping the sign of the current is analogous to the transition from stable equilibrium to unstable equilibrium (Fig. 2.3).

If there is no fluctuation at all, the DW will stay pinned at the modulation boundary even for the negative current since the net force on a DW is still zero (unstable equilibrium). However, since there are always fluctuations in a real world, the DW would depin to left or right depending on the direction of the initial fluctuation, no matter the origin. This bistable depinning behavior has been confirmed from the micromagnetic simulation. In the simulation, the DW always depinned to left/right under very small demagnetizing field facing left/right (with

every other conditions set to be the same).

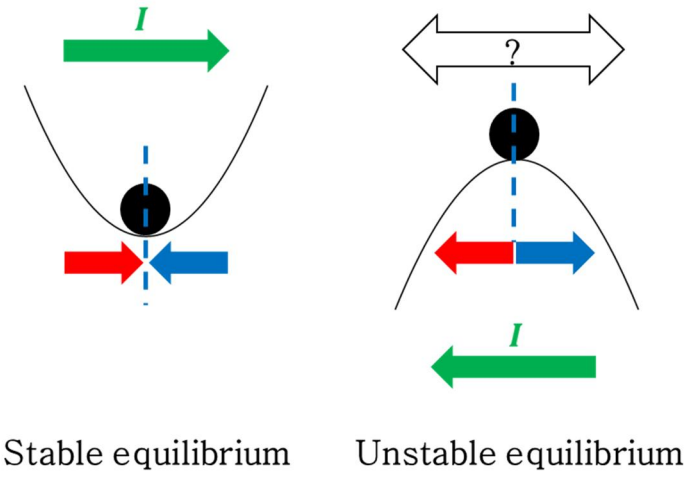

Figure 2.3 Schematics of energy state analogy for positive/negative current at the modulation boundary. The green arrow represents the electric current direction. The black dot represents the DW position. The red and blue arrow represents the SOT direction at each regions across the modulation boundary that are denoted as the blue dotted line.

The depinning itself is possible this way by negative electric current. The trouble is that the direction of the depinning depends on the initial fluctuation which is inconsistent. This is especially troublesome in realizing the racetrack memory with the modulation boundaries as described in Fig. 2.4. In this scheme, by alternating between positive and negative current, the DW should successively move across the modulation boundaries in same direction. However, in a real wire, since the DW moves through inherent random pinning sites, it is expected for a DW to stop slightly before the equilibrium point at the center of modulation boundary. Consequently, when the negative current is applied, the DW will depin backward along the arriving direction. This

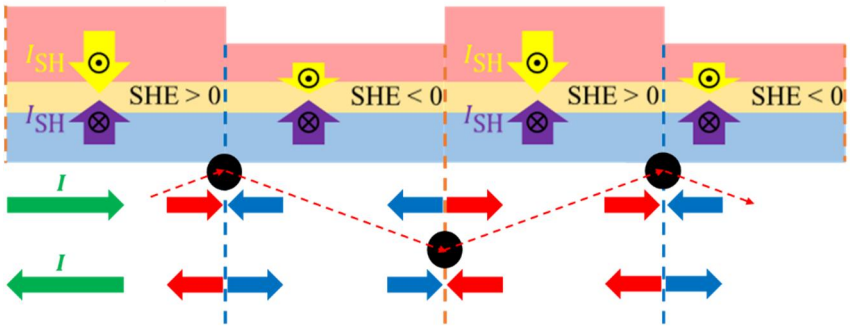

Figure 2.4 Schematics of a successive stepwise DW motion across the spin-Hall-effect-modulation boundaries by alternating current. The orange and blue dotted lines represent the modulation boundaries from thin to thick and thick to thin top layers respectively. Other symbols are set accordingly with the previous figures in chapter 2.

conclusively disables the successive stepwise unidirectional depinning of a DW across the multiple modulation boundaries. Hence, the reliable and systematic mechanism that can successively depin the DW in same direction is essential.

2.4 Unidirectional depinning at three different spin-Hall-effect-modulation boundaries

Producing unidirectional depinning mechanism is crucial. To accomplish this, one needs to invent a consistent way to slightly push the pinned DW in a certain direction. One more constraint is that this mechanism should work on both modulation boundaries (blue and orange dotted lines in Fig. 2.4) in a same direction. For instance, if one manufactures the thinner region in Fig. 2.4 to be preferred energetically

by a DW, the DW would depin to the right at the blue modulation boundaries but to the left at the orange modulation boundaries, eventually failing on successive unidirectional depinning.

After some trials and error, we came up with three possible models that can accomplish this. The micromagnetic simulation was used to verify if these proposed models satisfy the criteria. The first trial was to align a triangle notch with the modulation boundary. We positioned the modulation boundary between the start point and the bottleneck of a given triangle notch. Then the DW pinned at the modulation boundary experiences a slight force toward the bottleneck of a triangle notch due to the pinning potential of the triangle notch. The micromagnetic simulation verified this which is organized in the Fig. 2.5.

In Fig. 2.5, one can see that the DW pinned at the modulation boundary under positive current bends toward the triangle notch. Since the unstable equilibrium breaks toward right due to the bent DW, the DW depins rightward under the negative current. Therefore, by aligning the triangle notches with the modulation boundaries in this way, the unidirectional successive stepwise motion can be realized.

Note here that the modulation boundary is positioned at the right half of the wire intentionally, since the demagnetizing field pushes the DW toward the center of the wire, so that the DW depins to the left without any modifications (in this case, the aligned notch). The fact that the DW depins to the right overcoming the demagnetizing field means that this aligned-notch model certainly depins the DW to the right and

the depinning direction was not decided randomly but systematically toward the notch. This method of proof is applied to following models too.

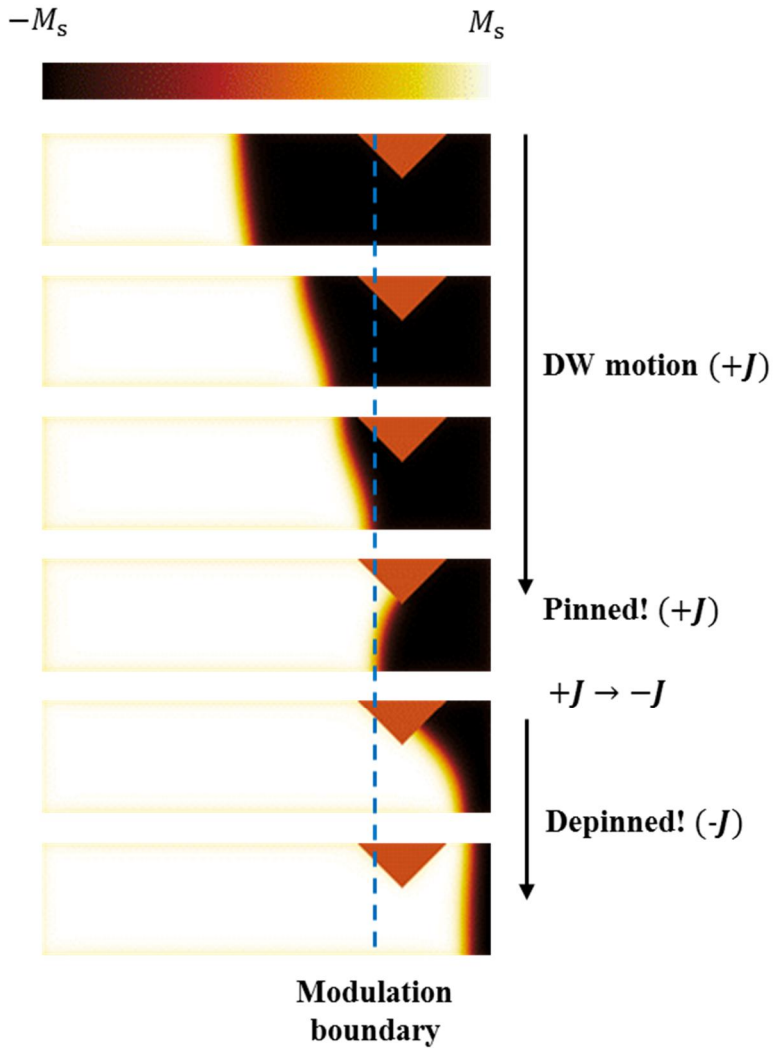

Figure 2.5 Micromagnetic simulation result of a unidirectional depinning from SHE-modulation boundary aligned with a triangle notch. The z component of the magnetization is illustrated with the color bar at the top with minimum/maximum value as the saturation magnetization, $\pm M_S$. The boundary between the up (white) and down (black) domains is the DW. The orange triangle is the notch. Other symbols are same.

Although the aligned-notch scheme provides one possible solution, the necessity of a geometric notch and that it should be aligned exactly at the point makes the solution less tempting for device application. Therefore, we focused on a model that can work without the notch. The following second trial was to change the modulation boundary from a perpendicular line into an arrow-shaped lines as illustrated in Fig. 2.6. However, the DW here depinned to the left which indicated that the depinning direction was decided by the base leftward demagnetizing field. Since the DW pins at the point where the force on a DW is split half and stays the same for negative current, the unstable equilibrium does not break by the arrow shape, and consequently the DW depins leftward.

This was solved by introducing an edge-pinning effect into the simulation. In a matter of fact, it is much more realistic to include the edge pinning in the picture. In most fabricated wires, the DW tends to move slower near the edge due to the irregularities found on the edges of the wire. Since the edge pinning is not systematically reproducible and has random nature, it is hard/impossible to precisely reproduce the strict edge pinning in the micromagnetic simulations. However, one can at least simulate and compare the cases of with or without the edge pinning. Surprisingly, the arrow-shaped modulation boundary with the edge pinning successfully depinned the DW to the right (Fig. 2.7). The edge pinning here was realized by introducing several small triangle notches along the wire edge. When the negative current is applied, the DW segment near the edge experiences the edge pinning that hinders the

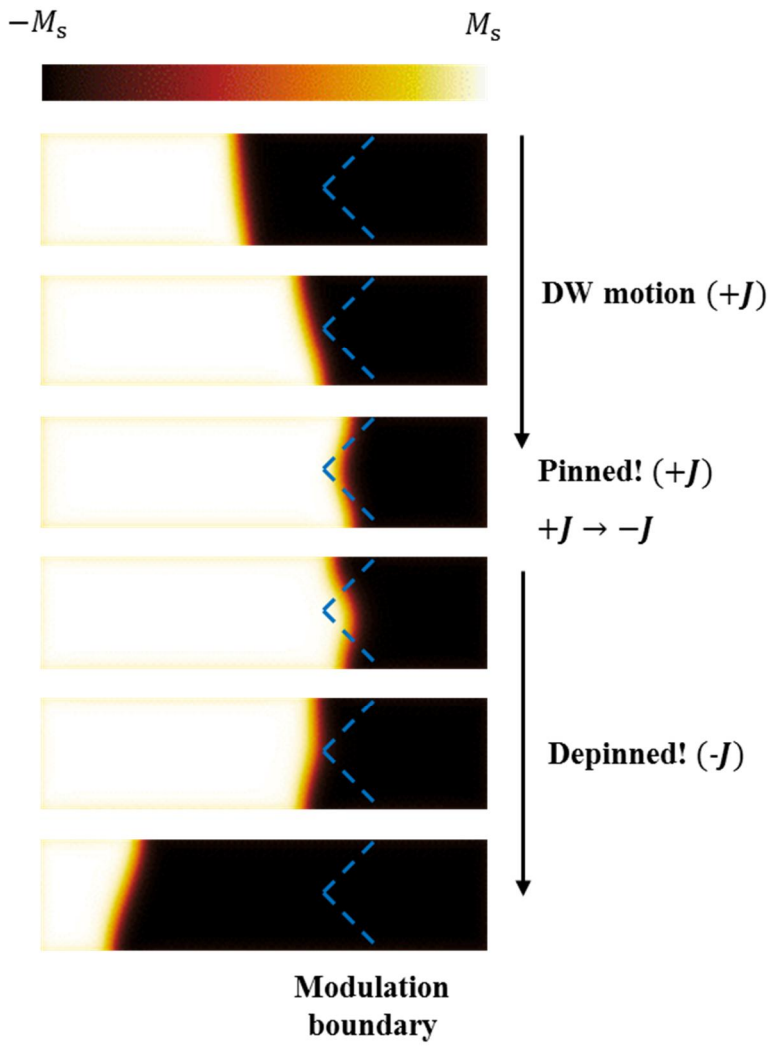

Figure 2.6 Micromagnetic simulation result of a depinning from arrow-shaped SHE-modulation boundary. Same notations and symbols.

leftward motion, while the DW segment near the center is driven rightward without any hindrances. Therefore, due to the edge pinning that slightly breaks the unstable equilibrium to the right, the DW can depin rightward.

Albeit the successful result, it is still not favorable to utilize the unsystematic edge pinning as part of the mechanism. It would be better

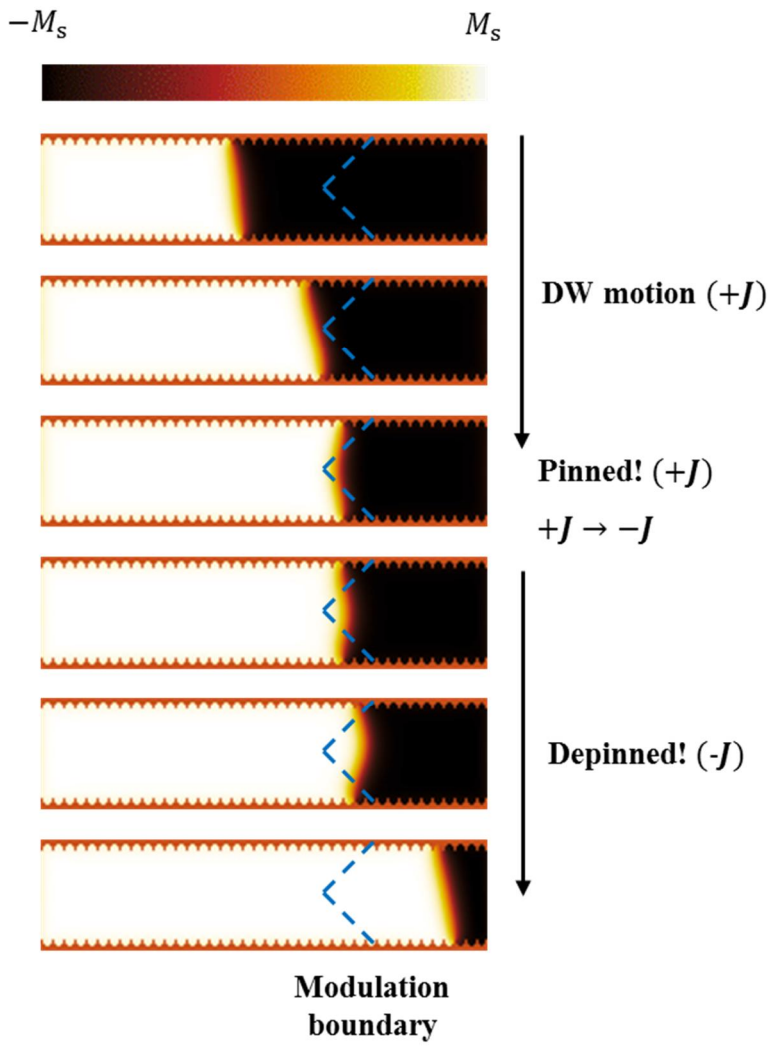

Figure 2.7 Micromagnetic simulation result of a depinning from arrow-shaped SHE-modulation boundary with edge pinning sites. Same notations and symbols.

if all the criteria can be met without either a notch or edge pinning sites. The last trial thus was to accomplish this only by shaping the modulation boundary properly. However, for most cases as the case of arrow-shaped modulation boundary, as the DW stops at the half point, the unstable equilibrium could not be broken by mere shape.

To overcome this, we configured a special shape utilizing the

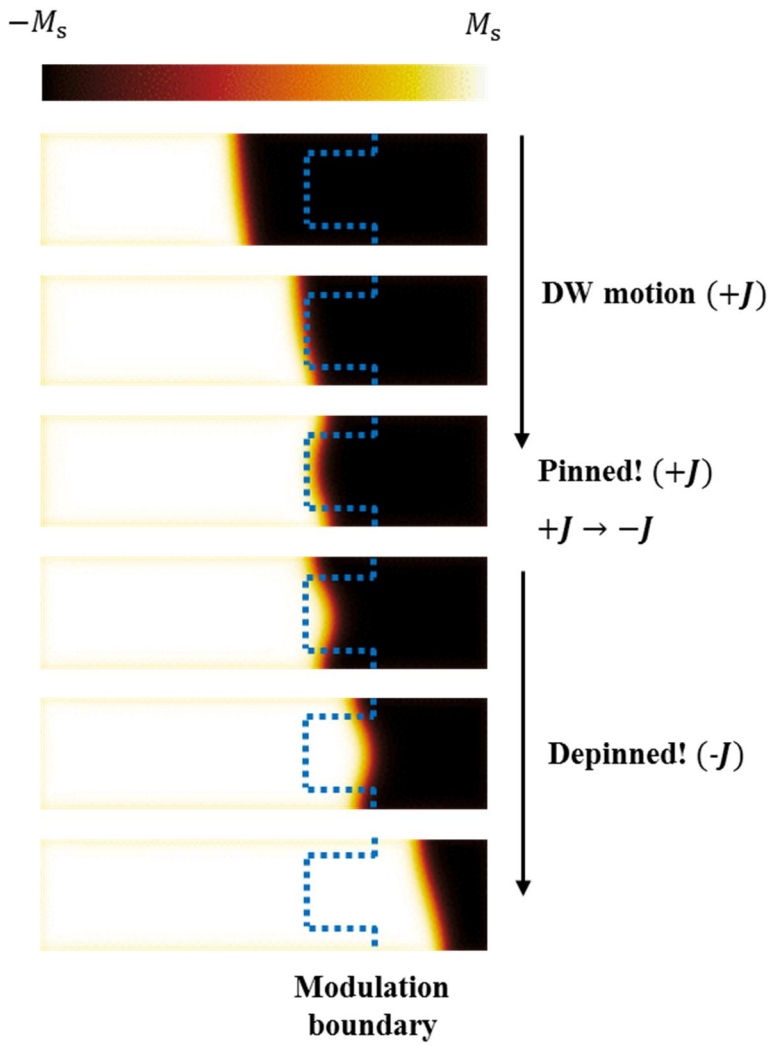

Figure 2.8 Micromagnetic simulation result of a depinning from step-function SHE-modulation boundary. Same notations and symbols.

step functions so that there is no point where a DW can be split half across the modulation boundary. By making the left section of the step modulation boundary longer than the section on the right, the DW can depin to the right systematically as illustrated in Fig. 2.8 and 2.8.

The mechanism of step-function modulation boundary model is simple. As can be seen in the third picture of Fig. 2.8, the DW is first

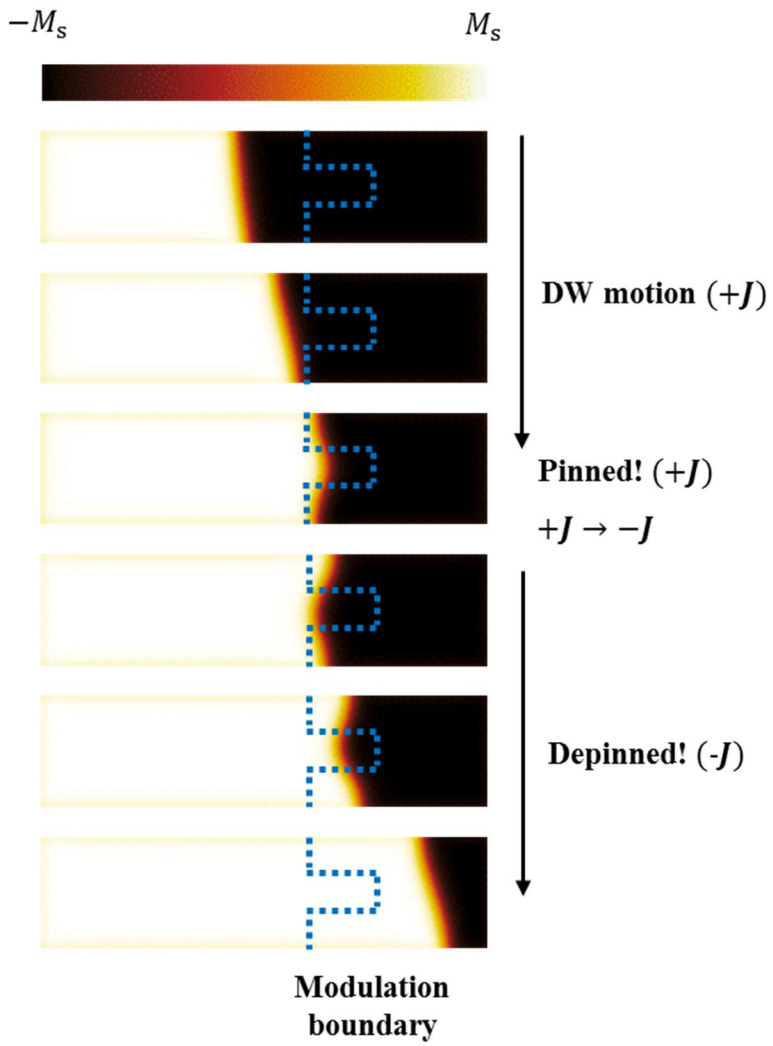

Figure 2.9 Micromagnetic simulation result of a depinning from step-function SHE-modulation boundary. Same notations and symbols.

balanced at the point where the leftward and rightward force is in equilibrium through the DW tension that shrinks the DW length along the DW. When the force direction is reversed for negative current, the middle and top/bottom sections of a pinned DW now moves separately at the instance. This is because the DW tension, that remains the same direction, no longer mediates the cancellation between forces on middle

and top/bottom sections of an elongated DW. Consequently, the middle section of the DW is absorbed completely into region at the right of the modulation boundary, while the top/bottom section just moves slightly to the left. Since the DW now sits in the region where the rightward force is larger than the leftward force due to the longer section length of the given step-function modulation boundary, the DW breaks from the unstable equilibrium and depins to the right. The same happens for Fig. 2.9 only with the top/bottom sections as the equilibrium breaker.

These 3 models that are the modulation boundary aligned with a notch, the arrow-shaped modulation boundary with edge pinning sites and the step-function modulation boundary, all provide a reliable way of unidirectional depinning, which makes the successive stepwise unidirectional DW motion in Fig. 2.4 possible. All three models are being fabricated by a fellow researcher, S. H. Lee and the aligned-notch model has already been verified to work properly by Y. S. Nam recently. These results will be published when enough experimental evidences are gathered. Hopefully, the result will provide a new way to pin/depin and control the DW motion.

Chapter 3. Spin-Hall-effect-modulation skyrmion oscillator

With the rapid expansion of global telecommunications in various frequency bands, it became necessary for a single mobile device to be equipped with multiple oscillators of different frequency bands. In order to avoid such complexity, numerous efforts have been devoted to developing an oscillator with high frequency tunability. Despite its promising start as a candidate for such an oscillator and a decade of studies to date, spin-torque oscillators still face problems regarding power output, linewidth, and magnetic-field-free operation. We propose here an entirely new concept of spin-torque oscillator, based on magnetic skyrmion dynamics subject to lateral modulation of the spin-Hall effect. As described in this chapter, the SHE-modulation skyrmion oscillator (SHEM-SO) is inherently safe from all the problematic issues of conventional spin-torque oscillators. We also believe that introducing this particular way of playing with the SHE modulation, combined with the super-fast dynamics of a skyrmion in a synthetic ferrimagnetic system, will further evoke various possibilities to the brains of spintronics. Therefore, the SHEM-SO can open a new chapter not only for a spin-torque oscillator but also for the undiscovered academic field of exotic spin dynamics in lateral SHE-modulation structures.

3.1 Introduction

The interaction between conduction electron's spin and the local magnetization, mediated by the spin torque [2-6], enabled the magnetization to be controlled electrically, which led to numerous key concepts of spintronic devices. Utilizing the steady–state spin precession of the magnetization under spin–polarized current, a nanoscale GHz–range tunable spin–torque oscillator [6,44-46] was one of those promising concepts. Albeit successful proof of principles to date, the spin–torque oscillators still suffer from issues regarding output power, linewidth and magnetic–field–free operation. Here we propose an entirely new concept of spin–torque oscillator, based on magnetic skyrmion dynamics subject to lateral modulation of the spin–Hall effect. In the oscillator, a skyrmion circulates around the modulation boundary between opposite SHE–torque regions, where the SHE pushes the skyrmion conversely toward the modulation boundary. A micromagnetic simulation confirmed such oscillations with frequencies of up to 15 GHz in media composed of synthetic ferrimagnets. This fast and robust SHE–modulation–based skyrmion oscillator is expected to overcome the issues associated with conventional spin–torque oscillators**.**

Spin–torque oscillators offer promising applications such as wide–range–tunable frequency generation/detection [47,48], signal processing [49], and dynamic recording [50]. The spin–torque nano–oscillator (STNO) [6,44-46] was the first example, which utilizes the spin precession induced by the spin–polarized current passing through

the point contact. Despite a successful demonstration of its high oscillation frequency with wide–ranging tunability [6,44-46], the STNOs still require improvement of their output power and linewidth, as well as their method of magnetic–field–free operation [51]. To overcome these issues, techniques such as synchronization between multiple point contacts [52] and self–injection locking [53] have been investigated. Otherwise, an enhanced output power with a much narrower linewidth has been attained by a spin–torque vortex oscillator (STVO) [54,55], which utilizes the gyration of a vortex core, confined within a point contact. By replacing the vortex core with a magnetic skyrmion, the concept of a spin–torque skyrmion oscillator (STSO) [56,57] has also been suggested, which would further improve the output power and be able to operate without an external magnetic field.

The narrow linewidth of the STVOs and STSOs is inherently attributed to the larger magnetic volume involved in the gyration [54]. However, the resulting frequencies are limited up to a maximum of a few GHz, which is much lower than the STNOs [54-57]. To increase the frequencies, it is essential to improve the speed efficiency of the vortex and skyrmion to the external current. Recently, many studies have reported on faster domain walls and skyrmions at the angular–momentum–compensation points of synthetic ferrimagnetic (SFi) systems [39-41]. However, since the gyrational torque vanish at the compensation point, applying SFi systems to conventional gyration based spin–torque oscillators is not possible. Therefore, to attain higher frequencies via the SFi system, it is necessary to build an entirely new

spin–torque oscillator, driven directly by the SHE torque rather than the gyrational torque.

3.2 Skyrmion motion at the tilted spin-Hall-effect modulation boundary

Herein, we propose new spin–torque oscillator—namely, the spin–Hall–effect–modulation skyrmion oscillator (SHEM–SO)—utilizing skyrmion motion directly driven by the SHE torque. We demonstrate that the SHEM–SO with a SFi system, produces a high frequency comparable to the STNOs, while maintaining the narrow linewidth of the STVOs.

Figure 3.1a is a schematic illustration of the spin–Hall current being injected from adjacent nonmagnetic (NM) layers into the ferromagnetic (FM) layer. Upon the injection of an electric current (I), the top and bottom NM layers generate vertical spin–Hall current (I_{SH}) of opposite spin polarizations [26,58]. The counterbalance between the I_{SH} of each NM layer determines the net spin polarization injected into the FM layer. Since the amount of I_{SH} depends on the thicknesses of the NM layers [26,27], it is possible to control the sign of the net spin polarization by adjusting the thicknesses of the NM layers, as exemplified by the two tri–layered structures with thicker and thinner top NM layers. These two structures experience opposite signs of net spin polarization and consequently opposing SHE torques (Fig. 1b).

Due to the skyrmion–Hall effect [59,60], the gyrational torque tilts the skyrmion trajectories by the skyrmion–Hall angle (θ_{SkH}) from the driving force direction (Fig. 3.1c). Note that these skyrmion trajectories are bound to opposite sides of the wire. Due to these reversed tendencies to the wire sides, if these two structures are joined as shown in Fig. 3.1d, it becomes possible for a skyrmion to form a closed oscillation path around the modulation boundary. We named this system "SHEM–SO".

A micromagnetic simulation was performed to confirm this prediction. The skyrmion indeed exhibited closed steady–state oscillation around the modulation boundary (Fig. 3.1e). The simulation also confirmed that a skyrmion converges to a single steady–state oscillation path regardless of its initial position.

The key features of the SHEM–SO are the non–zero θ_{SkH} and the tilted modulation boundary with an angle (θ_{B}). Depending on the relation between θ_{SkH} and θ_{B}, two distinctive oscillation paths appear. Figure 3.2 depicts (a) the parallelogram–like path for $\theta_{\mathrm{SkH}} \geq \theta_{\mathrm{B}}$ and (b) the parallel path along the modulation boundary for $\theta_{\mathrm{SkH}} < \theta_{\mathrm{B}}$, respectively.

For $\theta_{\mathrm{SkH}} \geq \theta_{\mathrm{B}}$, the SHE torque exerts a driving force on the skyrmion in the direction of the electric current and then, the skyrmion moves in the direction at an angle θ_{SkH} from the $\vec{F}_{\mathrm{SHE}}$ (Fig. 3.2c). As the skyrmion approaches the edge, the edge repulsion force ($\vec{F}_{\mathrm{edge}}$)

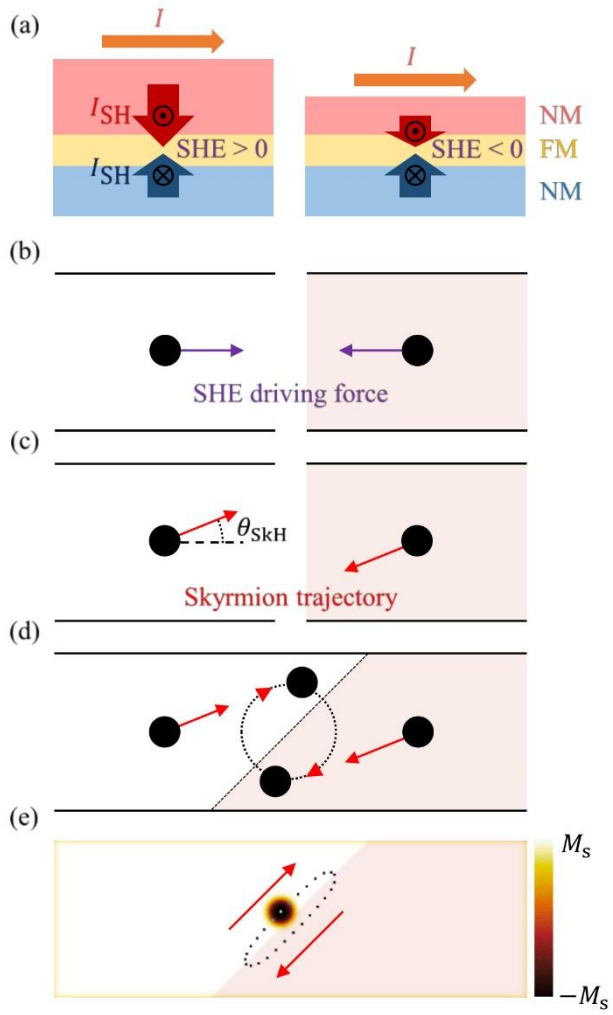

Figure 3.1 SHEM-SO operation principle. **a**, Cross–sectional view of layered structure with SHE modulation. The red, yellow, and blue areas indicate the top NM, FM, and bottom NM layers, respectively. The orange arrows show the direction of $\boldsymbol{I}$. The red and blue arrows are the directions of $\boldsymbol{I}_{\mathrm{SH}}$ from the top and bottom NM layers, respectively. **b**, Top view of each layered structure. The white and light–pink areas indicate the regions of the opposite SHE signs. The black circular dots represent skyrmions. The purple arrows show the SHE–induced driving forces. **c**, The red arrows show the skyrmion trajectories with an angle $\boldsymbol{\theta_{SkH}}$. **d**, Schematic of closed skyrmion path in conjoined SHE modulation structure. **e**, Simulation result of steady–state skyrmion oscillation. The color corresponds to the out–of–plane component of the magnetization as indicated by the color bar on the right.

increases until the skyrmion moves parallel to the edge (Fig. 3.2d). When

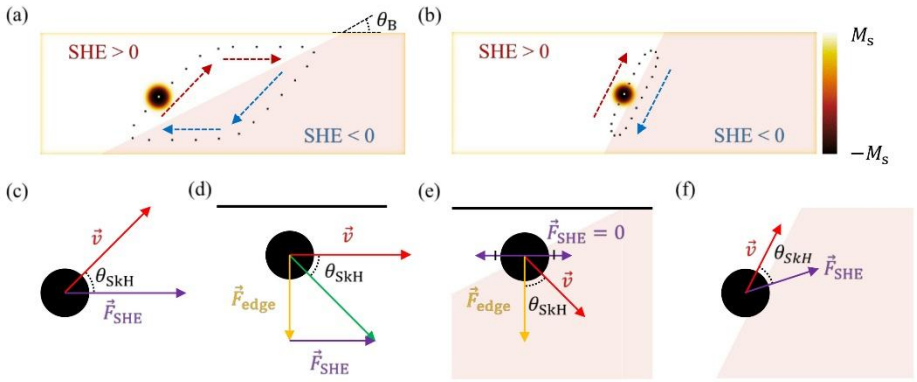

Figure 3.2 Simulated skyrmion paths and schematics of skyrmion dynamics in each process. Simulated results for skyrmion oscillation paths for a, $\theta_{SkH} > \theta_B$ and b, $\theta_{SkH} < \theta_B$. The white and light–pink areas indicate the regions of the opposite SHE signs, modulated by an angle θ_B. Schematics of skyrmion dynamics for the areas: c, far away from the modulation boundary, d, near an edge, e, near an edge and modulation boundary, and f, along the modulation boundary. The purple, yellow, and red arrows indicate the directions of the $\vec{F}_{SHE}$, $\vec{F}_{Edge}$, and skyrmion velocity ($\vec{v}$). The black horizontal lines in d and e represent the upper edge of the wire.

the skyrmion reaches the modulation boundary, the $\vec{F}_{SHE}$ starts to decrease due to the cancellation between the opposite SHE regions and the skyrmion drifts away from the edge by $\vec{F}_{edge}$ (Fig. 3.2e). The same processes repeat in the opposite SHE region to form a closed path.

For $\theta_{SkH} < \theta_B$, the skyrmion first reaches the modulation boundary. The net $\vec{F}_{SHE}$ at the modulation boundary now tilts away from the electric current direction until the trajectory becomes parallel to the modulation boundary (Fig. 3.2f) (see Supplementary chapter after). Then, upon approaching the wire edge, $\vec{F}_{edge}$ pushes the skyrmion into the opposite SHE region (Fig. 3.2e). The same processes repeat in the

opposite SHE region to form a closed path.

3.3 Properties of the SHEM-SO

The main properties of the SHEM–SO as an oscillator is discussed here. The length of the oscillation path and the skyrmion speed along the path determine the oscillation frequency (f). For heuristic reasons, θ_{B} is fixed to 45°, since f is a slow varying function of θ_{B} with a maximum near $\theta_{\mathrm{B}} \cong 45°$ (see Supplementary chapter after). Since the oscillation path is confined within the wire, the path length directly depends on the wire width (w) and therefore, a narrower wire is preferred for a higher f. The simulation results confirm that f is inversely proportional to w over a range down to the practical lower limit (around 50 nm), close to the skyrmion size (Fig. 3.3a).

Figure 3.3b–d illustrates the simulated oscillation paths for different values of w. Note that, as the w decreases, the skyrmion motion becomes more confined, but still exhibits an elliptical path, elongated along the wire length. Putting a magnetic tunnel junction (MTJ) nano–pillar structure on the tip of the elliptical path makes it possible to detect a large output signal with the skyrmion motion across the nano–pillar. Alike the STVOs, the large magnetic volume of the well–defined skyrmion structure is expected to provide a robust oscillation resulting in a narrow linewidth. Since the SHEM–SO operation naturally does not require external magnetic field, it is notable that the SHEM–SO can solve

all the issues of the conventional spin–torque oscillators, if only the GHz–range f can be acquired.

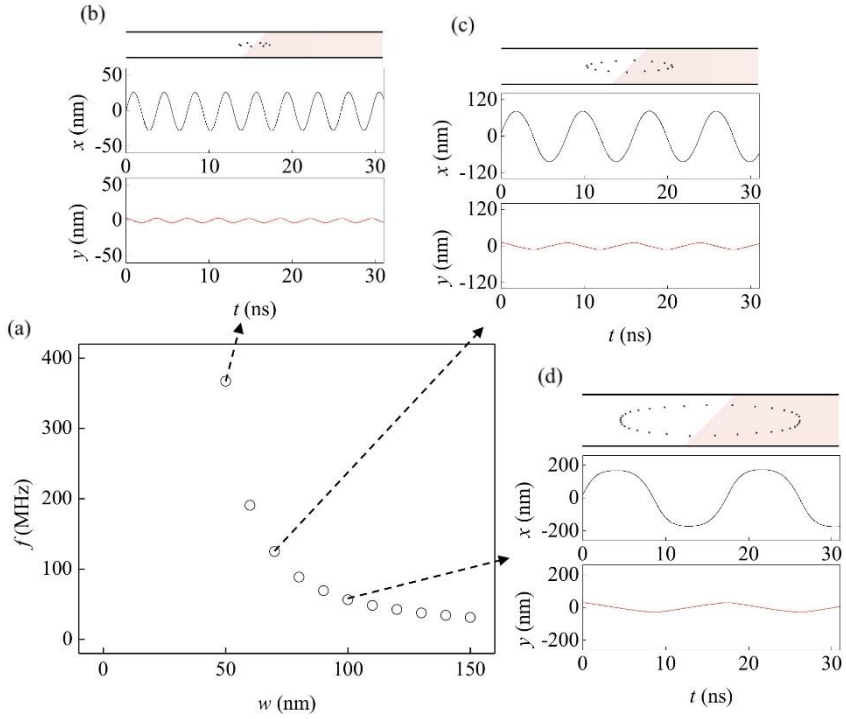

Figure 3.3 Oscillation frequency and paths with respect to wire width. a, Plot of f with respect to w. **b–d**, Oscillation paths and plot of the x and y positions with respect to time t for wires for which $w =$ 50, 70, 100 nm, respectively.

3.4 Spin-Hall-effect-modulation skyrmion oscillator in the synthetic ferrimagnetic structure

For fixed oscillation paths, the skyrmion speed determines f. Since the skyrmion motion is driven by the SHE torque by a DC current, a higher current density (J) leads to a faster skyrmion and consequently, a higher f. However, since J also increases the skyrmion–Hall force,

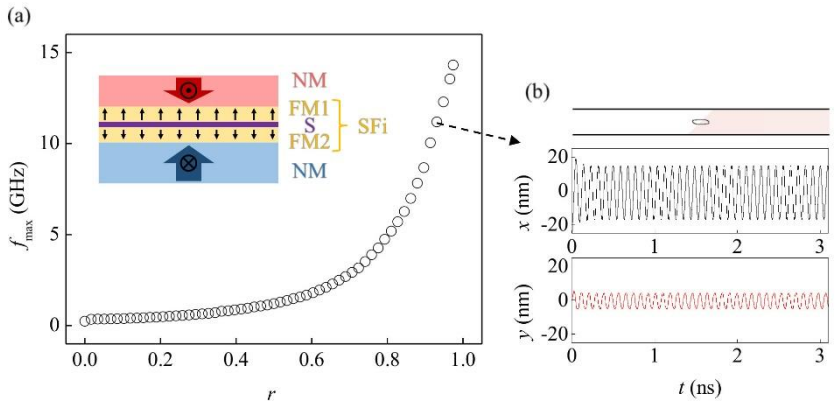

Figure 3.4 Oscillation frequency with respect to angular momentum ratio of synthetic ferrimagnet. a, Plot of $f_{\max}$ with respect to r. Inset illustrates the synthetic ferrimagnetic multilayer structure composed of two ferromagnetic layers (FM1 and FM2) and a spacer (S). b, Oscillation paths and plot of x and y positions with respect to time t for $r = 0.93$.

the skyrmions are destroyed at the wire edge for excessively large J. The maximum applicable current density ($J_{\max}$) is determined by the counterbalance between the skyrmion–Hall force and the edge–repulsion force. The maximum possible frequency ($f_{\max}$) is attained at $J_{\max}$.

To increase $f_{\max}$ further, the SFi system was adopted that are known to exhibit high DW/skyrmion speeds near the angular–momentum compensation point [39-41]. The SFi system consists of two FM layers with an antiferromagnetic coupling separated by a spacer. By controlling the compositions of the FM layers, the ratio r ($\equiv \gamma_2 M_{S1} t_1 / \gamma_1 M_{S2} t_2$) can be adjusted to reach the angular–momentum compensation condition (i.e. $r = 1$), where $\gamma_{1,2}$, $M_{S1,2}$, and $t_{1,2}$ are the gyromagnetic constants, saturation magnetizations, and thicknesses of the FM layers, respectively. As r approaches 1, the SHE–torque

efficiency increases considerably and the gyroscopic force eventually decreases to zero [39-41]. The former enhances the skyrmion speed while the latter enhances $J_{\max}$. Figure 3.4 clearly shows that $f_{\max}$ increases drastically as r approaches 1 and, $f_{\max}$ up to about 15 GHz is successfully demonstrated at $J_{\max} = 5.0 \times 10^{11}\ \mathrm{A/m^2}$, which corresponds to $30\ \mu\mathrm{A}$ through the magnetic layer.

3.5 Conclusion

We have proposed an entirely new concept of a spin–torque oscillator that is not based on gyration and thus can harness the state–of–the–art results of ultrafast spin dynamics in SFi systems. With the promising features regarding output power, linewidth and magnetic–field–free operation, the SHEM–SO can open a whole new chapter of designing nanoscale tunable microwave oscillators.

3.6 Supplementary

3.6.1 Simulation methods

A finite–element micromagnetic simulation was carried out using OOMMF code [42] with a Dzyaloshinskii–Moriya interaction (DMI) module [61]. For the tri–layered ferromagnetic films (Figs. 1–3), the FM layer thickness was set to 0.6 nm. Typical magnetic parameters of Pt/Co/Pt films were used [62], that are $580\ \mathrm{kA/m}$ for the saturation

magnetization, 15 $\mathrm{pJ/m}$ for the exchange stiffness, 0.8 $\mathrm{MJ/m^3}$ for the perpendicular magnetic anisotropy, and 3.5 $\mathrm{mJ/m^2}$ for the DMI strength. For the synthetic ferromagnetic films (Fig. 3.4), the thicknesses of the two FM and space layers were set to 0.4 nm. The same magnetic parameters as those of the above tri–layered ferromagnetic films were used, with the exception of the magnetization of the top FM2 layer, which varied from 0 to 580 $\mathrm{kA/m}$. The exchange stiffness between the layer [59] was set to -0.3 $\mathrm{pJ/m}$. For all the simulations, the lateral cell size was set to 1 nm. The damping–like spin–orbit torque efficiency from the SHE was set to $\pm 10^{-13}$ $\mathrm{Tm^2/A}$ for each opposite SHE region. The field–like spin–orbit torque was not included in the simulation. The current density varied over a range of 0.01 to 0.5×10^{12} A/m. The damping parameter was 0.01 in most cases, except in the case of Figs. 3.1 and 3.2 that utilized a value large enough to ensure the clear visualization of the oscillation paths.

3.6.2 Thiele formula for skyrmion motion near modulation boundary

When a Nèel-type skyrmion with cylindrical symmetry is driven by a driving force $\left(F_x^{\mathrm{ext}}, F_y^{\mathrm{ext}}\right)$, the steady-state velocity $\left(v_x, v_y\right)$ of the skyrmion is given by

$$\begin{pmatrix} v_x \\ v_y \end{pmatrix} = \frac{1}{(\alpha D)^2+G^2}\begin{pmatrix} \alpha D & G \\ -G & \alpha D \end{pmatrix}\begin{pmatrix} F_x^{\mathrm{ext}} \\ F_y^{\mathrm{ext}} \end{pmatrix}, \tag{3.1}$$

based on the Thiele formula of the Landau-Lifshitz-Gilbert equation, where α is the damping parameter, G is the integrated gyration term,

and D is the integrated dissipation term. By defining the skyrmion Hall angle θ_{SkH} as $\tan\theta_{\mathrm{SkH}} = -\frac{G}{\alpha D}$, the equation can be rewritten as

$$\begin{pmatrix} v_x \\ v_y \end{pmatrix} = \frac{1}{\sqrt{(\alpha D)^2+G^2}} \begin{pmatrix} \cos\theta_{\mathrm{SkH}} & -\sin\theta_{\mathrm{SkH}} \\ \sin\theta_{\mathrm{SkH}} & \cos\theta_{\mathrm{SkH}} \end{pmatrix} \begin{pmatrix} F_x^{\mathrm{ext}} \\ F_y^{\mathrm{ext}} \end{pmatrix}. \tag{3.2}$$

Eq. 3.2 indicates that a skyrmion moves in a direction with a fixed angle of θ_{SkH} from the external driving force, as discussed in the Fig. 3.2. The SHE-induced driving force under the injection of a current density J is then given by the integration over the entire film area A as

$$F_i^{\mathrm{SHE}} = -\gamma\epsilon_{\mathrm{SHE}} J \int \vec{m}_p \cdot \left(\frac{\partial\vec{m}}{\partial x_i} \times \vec{m}\right) dA, \tag{3.3}$$

where γ is the gyromagnetic ratio and ϵ_{SHE} is the SHE efficiency. Here, $\vec{m}$ is the unit vector of the magnetization in the FM layer and $\vec{m}_p$ is the unit vector of the spin polarization of the SHE electrons injected from the NM layers. In this formula, $\vec{m}_p$ is perpendicular to the direction of J within the film plane.

To estimate F_i^{SHE} across the modulation boundary, we assume rigid skyrmions composed of a Nèel-type domain wall with cylindrical symmetry and then, with some rewriting, the skyrmion texture can be expressed as a cylindrical coordinate (ρ, φ, z) as

$$\begin{pmatrix} m_\rho \\ m_\varphi \\ m_z \end{pmatrix} = \frac{N}{\cosh^2\left(\frac{l}{\lambda}\right)+\sinh^2\left(\frac{\rho}{\lambda}\right)} \begin{pmatrix} 2d\cosh\left(\frac{l}{\lambda}\right)\sinh\left(\frac{\rho}{\lambda}\right) \\ 0 \\ \cosh^2\left(\frac{l}{\lambda}\right) - \sinh^2\left(\frac{\rho}{\lambda}\right) \end{pmatrix}, \tag{3.4}$$

or as a Cartesian coordinate (x, y, z) as

$$\begin{pmatrix} m_x \\ m_y \\ m_z \end{pmatrix} = \frac{N}{\cosh^2\left(\frac{l}{\lambda}\right)+\sinh^2\left(\frac{\sqrt{x^2+y^2}}{\lambda}\right)} \begin{pmatrix} \frac{x}{\sqrt{x^2+y^2}}\left[2d\cosh\left(\frac{l}{\lambda}\right)\sinh\left(\frac{\sqrt{x^2+y^2}}{\lambda}\right)\right] \\ \frac{y}{\sqrt{x^2+y^2}}\left[2d\cosh\left(\frac{l}{\lambda}\right)\sinh\left(\frac{\sqrt{x^2+y^2}}{\lambda}\right)\right] \\ \cosh^2\left(\frac{l}{\lambda}\right)-\sinh^2\left(\frac{\sqrt{x^2+y^2}}{\lambda}\right) \end{pmatrix}, \tag{3.5}$$

where l is the skyrmion size and λ is the domain wall width. Here, d is the sign of the DMI and N is the topology number (= ±1) depending on the magnetic polarity inside the skyrmion. By applying the skyrmion texture defined by Eq. 3.4, the integration in Eq. 3.3 can be rewritten as

$$\tilde{F}_{x,y}^{\mathrm{SHE}} = -\gamma\epsilon_{\mathrm{SHE}}J\int_{-\infty}^{\infty}\int_{-\infty}^{\infty} f_{x,y}(x,y)dx\,dy, \tag{3.6}$$

where the force densities $f_x(x,y)$ and $f_y(x,y)$ are defined by

$$\begin{cases} f_x(x,y) = & 8\cosh\left(\frac{l}{\lambda}\right)/\left\{(x^2+y^2)\left[\sinh^2\left(\frac{\sqrt{x^2+y^2}}{\lambda}\right)+\cosh^2\left(\frac{l}{\lambda}\right)\right]^2\right\} \\ & \times\left\{\sinh^2\left(\frac{\sqrt{x^2+y^2}}{\lambda}\right)\left[x^2\cosh\left(\frac{\rho}{\lambda}\right)-\frac{l}{\sqrt{x^2+y^2}}y^2\sinh\left(\frac{\sqrt{x^2+y^2}}{\lambda}\right)\right]\right. \\ & \left.+\cosh^2\left(\frac{l}{\lambda}\right)\left[x^2\cosh\left(\frac{\sqrt{x^2+y^2}}{\lambda}\right)+\frac{l}{\sqrt{x^2+y^2}}y^2\sinh\left(\frac{\sqrt{x^2+y^2}}{\lambda}\right)\right]\right\} \\ f_y(x,y) = & 2xy\cosh\left(\frac{l}{\lambda}\right)/\left\{(x^2+y^2)\left[\sinh^2\left(\frac{\sqrt{x^2+y^2}}{\lambda}\right)+\cosh^2\left(\frac{l}{\lambda}\right)\right]^2\right\} \\ & \times\left\{\cosh^2\left(\frac{l}{\lambda}\right)\left[\cosh\left(\frac{\sqrt{x^2+y^2}}{\lambda}\right)-\frac{l}{\sqrt{x^2+y^2}}\sinh\left(\frac{\sqrt{x^2+y^2}}{\lambda}\right)\right]\right. \\ & \left.+\sinh^2\left(\frac{\sqrt{x^2+y^2}}{\lambda}\right)\left[\cosh\left(\frac{\sqrt{x^2+y^2}}{\lambda}\right)+\frac{l}{\sqrt{x^2+y^2}}\sinh\left(\frac{\sqrt{x^2+y^2}}{\lambda}\right)\right]\right\} \end{cases}, \tag{3.7}$$

in the case that J is injected along the x axis and thus, $\vec{m}_p$ is parallel to the y axis. Inside an area of uniform SHE, the integration of Eq. 3.6 gives $\tilde{F}_y^{\mathrm{SHE}} = 0$ and thus, the SHE-induced driving force is parallel to the current direction in the uniform SHE region.

When a skyrmion approaches the modulation boundary by a

normal distance δ, Eq. 3.6 is modified to

$$F_{x,y}^{\mathrm{SHE}}(\delta) = -\gamma\epsilon_{\mathrm{SHE}}J\left(\int_{-\infty}^{\infty}\int_{-\infty}^{x\tan\theta_{\mathrm{B}}} f_{x,y}(x-\delta\sin\theta_{\mathrm{B}}, y+\delta\cos\theta_{\mathrm{B}})dx\,dy - \int_{-\infty}^{\infty}\int_{x\tan\theta_{\mathrm{B}}}^{\infty} f_{x,y}(x-\delta\sin\theta_{\mathrm{B}}, y+\delta\cos\theta_{\mathrm{B}})dx\,dy\right), \quad (3.8)$$

where θ_{B} is the angle of the modulation boundary. Note that $\tilde{F}_{x,y}^{\mathrm{SHE}}$ in Eq. 3.6 equals $F_{x,y}^{\mathrm{SHE}}(-\infty)$ in Eq. 3.8. Figure 3.5.a plots the numerical calculation results of $F_{x,y}^{\mathrm{SHE}}$. The plots clearly show that F_x^{SHE} monotonically decreases to zero with δ. On the other hand, F_y^{SHE} increases from zero to a maximum and then vanishes as δ approaches to zero. Then, as shown in Fig. 3.5.b, the angle θ_{SHE} $(= \tan^{-1}(F_y^{\mathrm{SHE}}/F_x^{\mathrm{SHE}}))$ increases as δ decreases and eventually, converges to a certain angle. When θ_{SHE} becomes an angle $\theta_{\mathrm{B}} - \theta_{\mathrm{SkH}}$, the skyrmion moves parallel to the modulation boundary as described in Fig. 3.2.f.

3.6.3 Thiele formula for synthetic ferrimagnets

For synthetic ferromagnetic films, G is rewritten as

$$G = 4\pi N\frac{(\gamma_2 M_{\mathrm{s}1}t_1 - \gamma_1 M_{\mathrm{s}2}t_2)}{(\gamma_2 M_{\mathrm{s}1}t_1 + \gamma_1 M_{\mathrm{s}2}t_2)}, \quad (3.9)$$

when synthetic ferrimagnetic films are composed of two FM layers with a gyromagnetic ratio $\gamma_{1,2}$, saturation magnetizations $M_{\mathrm{s}1,2}$, and thicknesses $t_{1,2}$ for each FM layer, respectively. Since the steady-state skyrmion speed is proportional to $\frac{1}{\sqrt{(\alpha D)^2+G^2}}$, as given by Eq. 3.2, the skyrmion speed increases as G decreases and approaches zero when $\gamma_2 M_{\mathrm{s}1}t_1 \cong \gamma_1 M_{\mathrm{s}2}t_2$ near the angular-momentum compensation

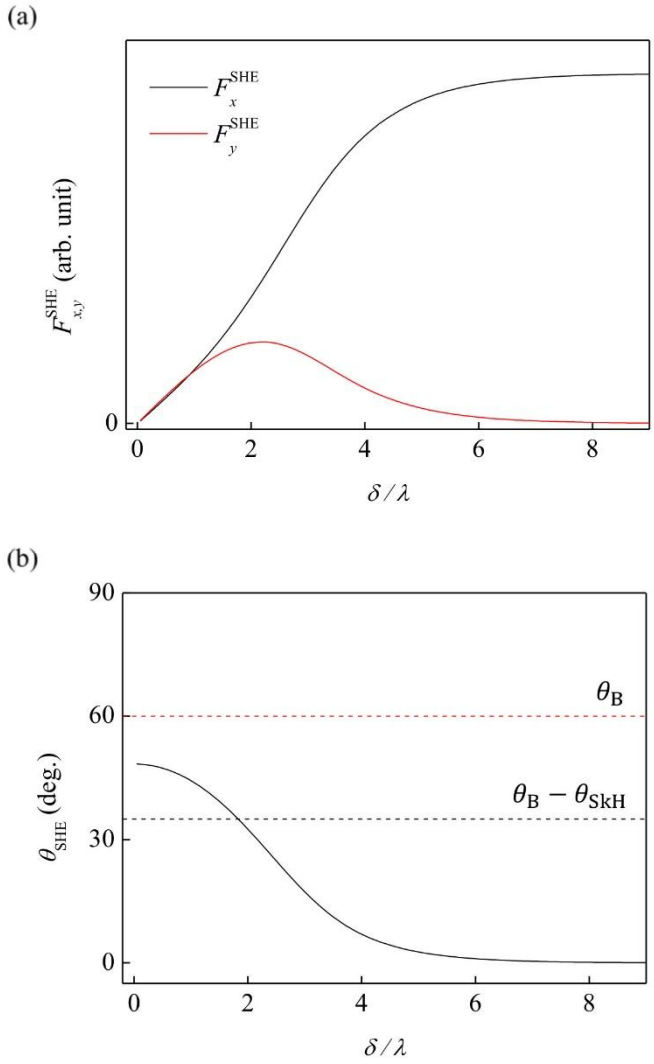

Figure 3.5 SHE force compensated at modulation boundary. a, Plot of $F_{x,y}^{\mathrm{SHE}}$ with respect to δ/λ. **b**, Plot of θ_{SHE} with respect to δ/λ. The red and black dashed lines show the values of θ_{B} and $\theta_{\mathrm{B}} - \theta_{\mathrm{SkH}}$.

condition. Under this condition, θ_{SkH} decreases to zero through the

Frelation $\tan\theta_{\mathrm{SkH}} \propto G$ and therefore, J_{max} increases with a reduction in the skyrmion-Hall-effect-induced gyroscopic force counterbalancing the edge repulsion force. Combining these two effects, the maximum

skyrmion speed and, thereby, $f_{\max}$, increases in the synthetic ferromagnetic films near the angular-momentum compensation condition.

3.6.4 Frequency variation with respect to the angle of the modulation boundary

As θ_B increases, f tends to increase since the overall path length decreases. On the other hand, as θ_B increases, f also tends to decrease since the skyrmion speed drops with larger compensation of the SHE force which comes from a smaller δ in the case of $\theta_B > \theta_{SkH}$ (Fig. 3.5.b). Due to the skyrmion size, this compensation also happens for $\theta_B < \theta_{SkH}$ near the edge and increases with θ_B. Therefore, a maximum f should appear due to the competition between these two tendencies.

Figure 3.6 confirms this prediction by plotting f with respect to θ_B for three different values of θ_{SkH}. The figure and various other results showed that the maximum value of f appears near $\theta_B \cong 45°$ and f varies slowly near its maximum value. This is the reason θ_B was chosen as 45° for simplicity throughout the chapter.

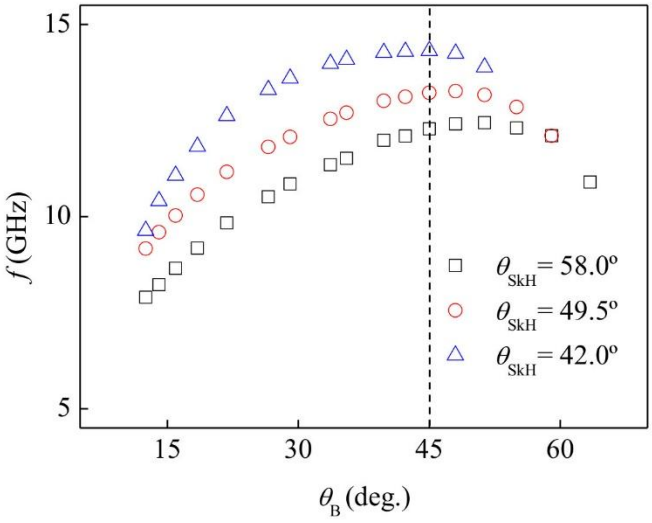

Figure 3.6 Frequency variation with respect to angle of modulation boundary. Plot of f with respect to θ_B for θ_{SkH} =58.0, 49.5, and 42.0°, respectively.

Chapter 4. Domain wall neuron device

Artificial intelligence is the critical keyword for a new age to come. As the computing technology develops exponentially, the 'faster' computing now stands for much more possibilities rather than mere convenience. Now, computers can be programmed to mimic the most human-like abilities from face recognition to the game of go. However, the computing systems based on Von-Neumann structure is on the edge of its capacity to be smaller and faster. The physical complexity to realize complex task-solving machine like Alpha-Go is too high compared to the much more efficient human brain that holds similar features. The artificial intelligence has to breakthrough this limit to function as effectively as (or more effectively than) its finest contender, human brain. There are already a lot of efforts being dedicated to accomplish this. One of the promising candidates that can provide the building block of an effective artificial intelligence is, of course, the spintronic devices. Due to the non-volatility of the magnetic memory, the base power requirement (that is too high at the moment) can be minimized ideally to zero. Furthermore, with previously discussed spin torques, the magnetic memory can be processed easily without separate processing unit as in the Von-Neumann architecture and thus the device can become much simpler. This chapter introduces one such spintronic device through CIDWM.

4.1 Introduction

Artificial intelligence (AI) is based on artificial neural network that essentially performs very complex mathematical fitting with countless fitting parameters. By tuning the multidimensional fitting parameters through a 'learning' process, a set of fitting parameters that can process a certain complex task, can be obtained. As in Eq. 4.1, every elements (w) in the matrices all correspond to the fitting parameters that is taught (tuned) to mimic complex human tasks.

$$(\text{Output}) = \begin{pmatrix} w_{11}^{N} & \cdots & w_{1n_N}^{N} \\ \vdots & \ddots & \vdots \\ w_{m_N 1}^{N} & \cdots & w_{m_N n_N}^{N} \end{pmatrix} \cdots \begin{pmatrix} w_{11}^{1} & \cdots & w_{1n}^{1} \\ \vdots & \ddots & \vdots \\ w_{m1}^{1} & \cdots & w_{mn}^{1} \end{pmatrix} \begin{pmatrix} a_1 \\ \vdots \\ a_n \end{pmatrix} \quad (4.1)$$

For example, a picture of hand-written number can be inserted as an input of the system. Consecutively after multiplying the associated fitting matrices, the output decides which number the hand-written image stands for. If enough pictures and corresponding answers are supplied to the system, the fitting parameters can be taught to recognize the hand-written numbers as humans do. When this learning process is complete, the fitting parameters now automatically convert the given image of a number to its corresponding value. In short, a very complex task of number recognition can be mimicked with many but finite fitting parameters and sufficient input (problem)-output (answer) data set.

The process of fitting can be understood more intuitively as a form of network (Fig. 4.1). Each matrix of Eq. 4.1 corresponds to the connection between the input/hidden/output layers (arrows between the

layers). The layers are associated with the elements of the input column, the intermediate columns (multiplied by the fitting matrices one-by-one) and the output column respectively. This picture is famous as the schematics of an artificial neural network.

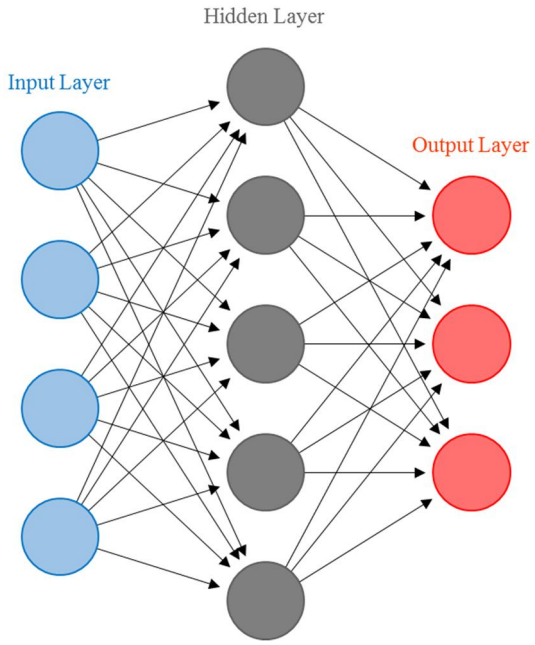

Figure 4.1 Schematics of an artificial neural network. The arrows represent the fitting matrix elements. The dots represent the input/intermediate/output column elements.

Physically, this form of artificial neural network can be realized with the crossbar structure in the Fig. 4.2. The resistance of the junction between horizontal and vertical bars acts as the fitting parameter that multiplies the input signal with according weight. The electric signals from the input layer is multiplied with their assigned matrix elements and summed out to the output layer.

Since the fitting parameter (weight) should be modifiable

throughout the learning process, the unit installed at the junction of a crossbar structure should have the so-called feature, ‘weight plasticity’. Additionally, since the unit at the output layer has to decide whether the net input signal is enough or not to trigger the output signal, the ‘integrate and fire’ feature is necessary. These units are called the synapse and neuron device respectively and mimic the actual role of the synapse and neuron in the biological neural networks.

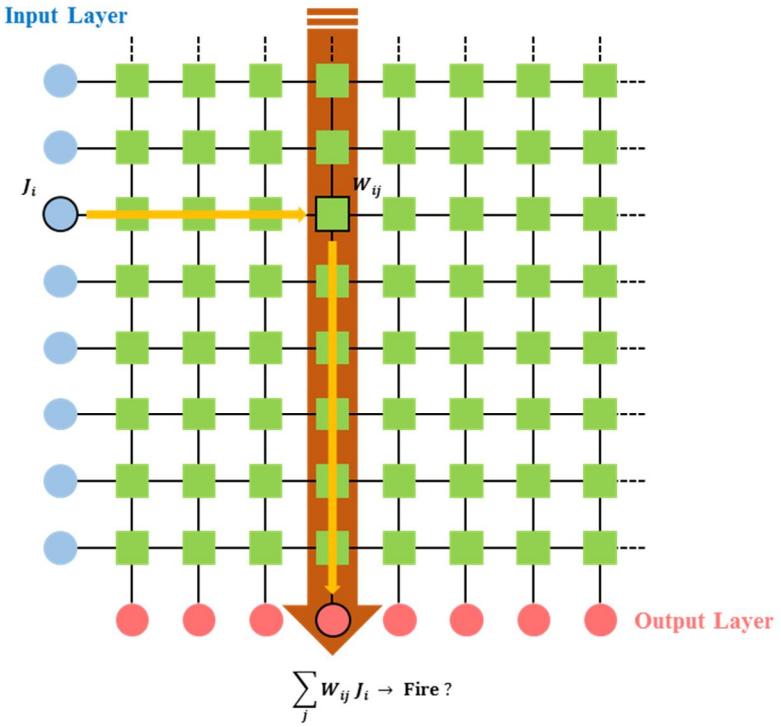

Figure 4.2 Schematics of a crossbar structure realizing an artificial neural network. The horizontal and vertical lines are conducting bars. The blue and red dots represent the input and output layer of an artificial neural network. The green square represents the junction with weight (resistance, $\boldsymbol{W_{ij}}$) between the horizontal and vertical conducting bars. The current $\boldsymbol{J_i}$ flows from the i^{th} input layer element to the j^{th} element of the output layer and gets multiplied by the weight at the junction.

As the task becomes more complex, the necessary number of synapse and neuron devices increases significantly to the point where the

whole system is much more complex and power consuming than the human brain performing the same task. Furthermore, for Von Neumann architecture that separates the processing unit and memory unit, there has to be separate processing and memory units for each synapse and neuron devices. This is the main reason the current artificial neural network is power consuming and complex.

Obviously, people try to design a synapse/neuron as simple and efficient as possible. All of these efforts to realize the artificial neural network that functions at the level of human-brain efficiency are summarized into a new field of study; namely, the neuromorphic engineering. Amongst various approaches, the spintronic devices stand out with their non-volatile memory feature. Since the non-volatile magnetization does not require ground voltage to maintain the memory, the base power consumption can be minimized. Furthermore, since the magnetic memory can be directly processed via the spin torques, the spintronic neuron and synapse devices hold a great potential to be the simplest and most power-efficient ingredients of the artificial intelligence.

4.2 Synapse device

Many spintronic synapse device ideas are already suggested in the field. The ‘weight plasticity’ feature is realized by the DW motion [63] and the skyrmion motion [64]. Basically, the whole idea is to modify

the magnetization under a magnetic tunnel junction to control the resistance. This feature is called the memresistance where the history of the current flow decides the resistance. As can be seen in the Fig. 4.3 [63], by controlling the DW position via horizontal current, the vertical resistance through a magnetic tunnel junction can be modified, which eventually realizes the weight plasticity. Since the DW stays at the same position under zero current, the base power consumption is zero. In addition, since the DW position can be directly modified via horizontal current, the processing unit is integrated with the memory unit in the simplest way possible.

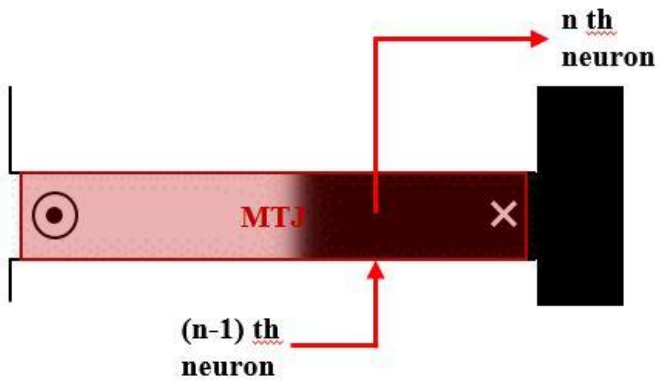

Figure 4.3 Schematics of a DW synapse device. The greyscale coloring represents the z component of a magnetization. The red square region represents the magnetic tunnel junction (MTJ) installed vertically. The red arrow shows the current flow through the MTJ to the next neuron layer.

4.3 Neuron device

Since the spintronic synapse devices are actively being studied

by others, we decided to focus on developing the spintronic neuron device. The integrate and fire feature of a neuron device can be realized by a lot of spintronic phenomena. Most commonly, the spin-torque oscillator can be utilized since the applied spin-polarized current pulses can be integrated to eventually flip the magnetization. The tilting by the current pulses corresponds to the integration of input signals and the complete switching of the magnetization corresponds to the firing of an output signal. However, as the spin-torque oscillator struggles to function at zero magnetic field, it would be great to accomplish other method.

In theory, any current-driven dynamics can be utilized as the neuron device, since the current pulses can be integrated into the state of the magnetization via spin torque. First, we tried various schemes utilizing a skyrmion motion, skyrmion generation, DW depinning and DW motion. The integrate and fire feature can easily be realized by any of these systems. For a spiking neural network that is being pointed out as further advanced generation of AI, a leaky integrate and fire feature is necessary. Since the data is stored as a form of spiking pulses, the gaps between spikes should be readable. For this case, the integration should be time dependent. This so-called ‘leaky integration’ can be realized by introducing a restoring force. However, for a static system that runs on a clock and does not require a ‘leaky’ feature, the simplest mechanisms would be the best.

The DW neuron device is very similar to the DW synapse device. Only the position of a magnetic tunnel junction is different. As illustrated in Fig. 4.4, the input current pulses are now integrated as the DW position.

When enough pulses are injected into the neuron device, the DW reaches the magnetic tunnel junction and the output signal is fired, whereas the insufficient pulses do not fire the output signal. When all the input pulses are injected and the output signal is fired/not fired, the DW is reset by the negative reset current to the initial pinning site and wait for the next iteration. Alike the synapse device, the processing unit is directly integrated with the memory unit that does not require any base power. With this DW neuron device idea, we acquired a related funding and the device is being fabricated with the help of fellow researchers.

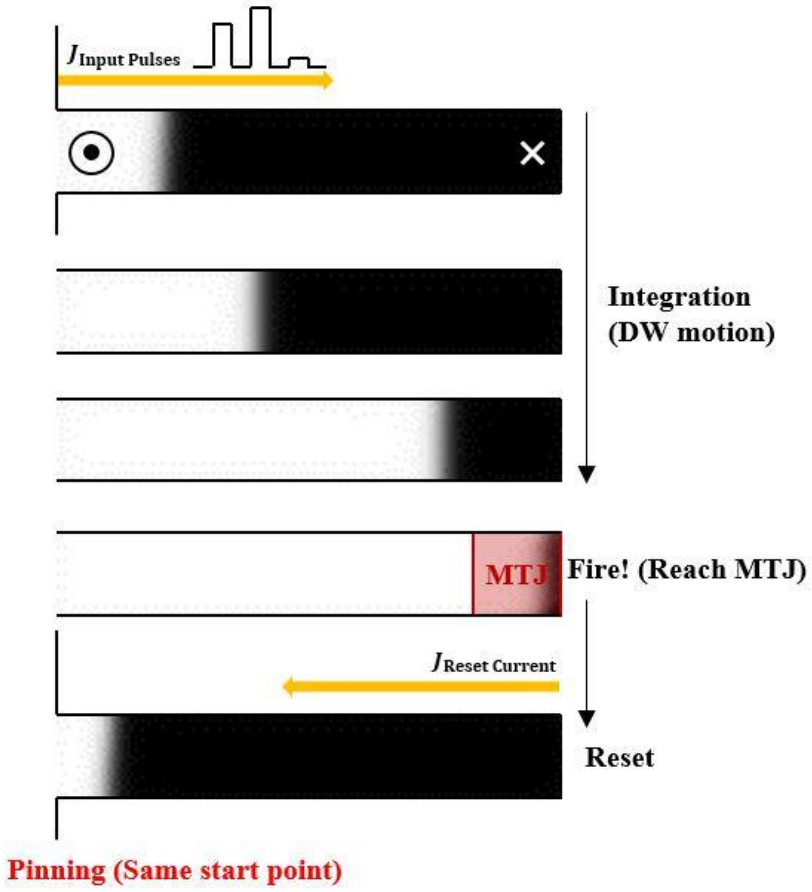

Figure 4.4 Schematics of a DW neuron device. Same notations and symbols with Fig. 4.3. The yellow arrows indicate the current flows.

Chapter 5. Derivation of miscellaneous analytic equations

Studies until chapter 4 have been mainly conducted on the micromagnetic simulation. Albeit the convenience of a numerical simulation, it would be always better if the system can be described by a simple analytic equation rather than by a complex numerical calculation that requires computing power. By obvious reasons, this case is rather rare. However, once the analytic equation is established, it becomes a powerful tool that provides the measurement principles, design rules and physical understandings. In this chapter, we explain the derivation processes of three analytic equations that are used to measure and predict associated magnetic properties.

5.1 The analytic formula on depinning current of magnetic domain walls driven by spin-orbit torques from artificial notches

Here, we present an analytic formula on domain-wall depinning current from artificial triangular notches driven by the spin-orbit torque combined with the Dzyaloshinskii-Moriya interaction. Interestingly, in contrast to the magnetic-field-driven depinning, the depinning current is governed solely by the notch slope angle, irrespective of the notch depth and wire width. An analytic formula is proposed to explain the present observation based on the variational principle for minimum energy states. The validity of the formula is verified via micromagnetic simulation, confirming the detailed effects of the spin-orbit torque and Dzyaloshinskii-Moriya interaction strengths.

The magnetic domain-wall (DW) motion along ferromagnetic nanowires has drawn vast technological attention due to its potential application toward logic and memory devices [65,66]. These devices store the digital data in the form of DWs and thus, for better performance, it is crucial to precisely control the positions of the DWs. There are several ways to accomplish this [67-69], but it is common to introduce artificial notches on the magnetic wire, at which the DWs are positioned by pinning [70-72]. Therefore, the DW pinning and depinning characteristics at notches have long been analyzed. For the magnetic-field-driven case, an analytic formula of the depinning magnetic field has been proposed as a function of the geometry of the notches [73]. However, recent discoveries of the current-driven DW motion demand

the reexamination of the DW pinning and depinning characteristics for the relevant DW driving mechanisms with the spin-orbit torque (SOT) and Dzyaloshinskii-Moriya interaction (DMI) [74-79]. In this chapter, we present an analytic formula of the depinning current for the case of SOT-driven DW depinning. An analytic model that explains the detailed pinning and depinning mechanisms is provided. The validity of the analytic model is verified by micromagnetic simulation.

5.1.1 Depinning field/current from a notch

Here, a nanowire with a single isosceles-triangular notch is studied. The geometry of a typical nanowire is illustrated in Fig. 5.1. The isosceles-triangular notch positioned on one edge of the nanowire has a depth d and angle θ. The width w of a nanowire ranges from 80 to 160 nm with a fixed thickness t (=0.3 nm). A nanowire is considered infinitely long, so that the simulation is carried out only on the center of a sufficiently long wire. The dipolar field from the 'missing' magnetization outside the simulation area is calculated beforehand using the volume average demagnetizing tensor of rectangular prism and included in the simulation as an external magnetic field [80]. The simulation cell size is chosen to be 2.5 nm, sufficiently smaller than the exchange length (~5 nm).

To simulate the current injection through the nanowire, the distribution of the current density is calculated considering the geometry of a notched wire. The steady-state solution of the distribution is obtained by applying the Kirchhoff's circuit laws recursively over the network of

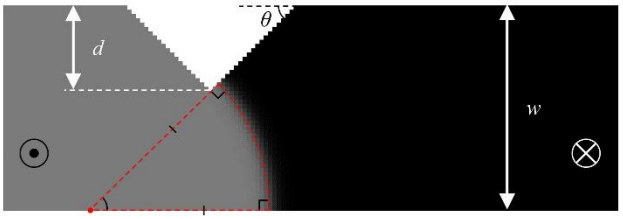

Figure 5.1 Schematics of a nanowire structure. The symbols d, w, and θ represent the notch depth, wire width, and notch angle, respectively. The gray-contrast image shows the snapshot of a DW just before depinning, between up (gray) and down (black) domains. The dashed red arc shows that the DW forms a circular arc with perpendicular intersections on both ends.

registers connecting the nearest neighbor cells of a rectangular mesh. Starting from the uniform current density distribution, the excess-current at the nodes of notch-boundaries gets redistributed to the remaining branches according to the Kirchhoff's first and second laws. Since the redistribution transfers the excess-current to their nearest neighbors, it happens recursively until the excess-current on every node converge to zero. The converged current distribution is applied to the micromagnetic simulation. Due to the non-uniform distribution of the current density, hereafter we use the total current I as the representative parameter of the injected current. The overall current density J can be then easily calculated from I by dividing by the wire width and the film thickness, i.e. $J = I/wt$.

The typical magnetic parameters of Pt/Co films are used for the saturation magnetization (=1.4×10^6 A/m), exchange stiffness (=3.1×10^{-11} J/m), and effective perpendicular magnetic anisotropy (=8.7×10^5 J/m^3) throughout the simulation [81,82]. For the SOT-induced DW motion,

various strengths of the longitudinal SOT efficiency β_L and the transverse SOT efficiency β_T from 0 to 2.4×10^{-13} Tm^2/A are used [83]. DMI strengths, D were varied within the range from 0.5 to 2.0 mJ/m^2 [84].

The micromagnetic simulation was performed by use of the object oriented micro magnetic framework (OOMMF) with the addition of external DMI and SOT modules [42,61]. A single vertical DW is initially placed at the tip of the triangular notch. The equilibrium state is then obtained for each stage of increasing I with an increment of 1.0×10^{-7} A. The condition that the maximum $|dm/dt|$ is smaller than 0.1 deg./ns is used as the criterion of the equilibrium state, where m is the unit magnetization of each cells. To decrease the simulation time, a relatively large value of the Gilbert damping parameter (=0.5) is used. As I reaches a certain threshold value, the DW depins from the notch. We denote the depinning current I_{dep} as the minimum I required for the DW depinning. The I_{dep} is obtained repeatedly for various values of w, d, θ, $\beta_{L/T}$, and D.

The case of purely-longitudinal-SOT-driven DW depinning (i.e. $\beta_T = 0$) is first examined with a fixed nonzero D (=1.0 mJ/m2) and β_L (=1.0×10-13 Tm2/A). The value of D is chosen large enough to induce the Néel-type DW. Figure 5.2 plots the simulation results of I_{dep} with respect to (a) d and (b) w for three different θ s. It is surprising to see that I_{dep} is unchanged irrespective of both d and w. Strictly, since a DW tends to ignore impurities smaller than the DW width, I_{dep}

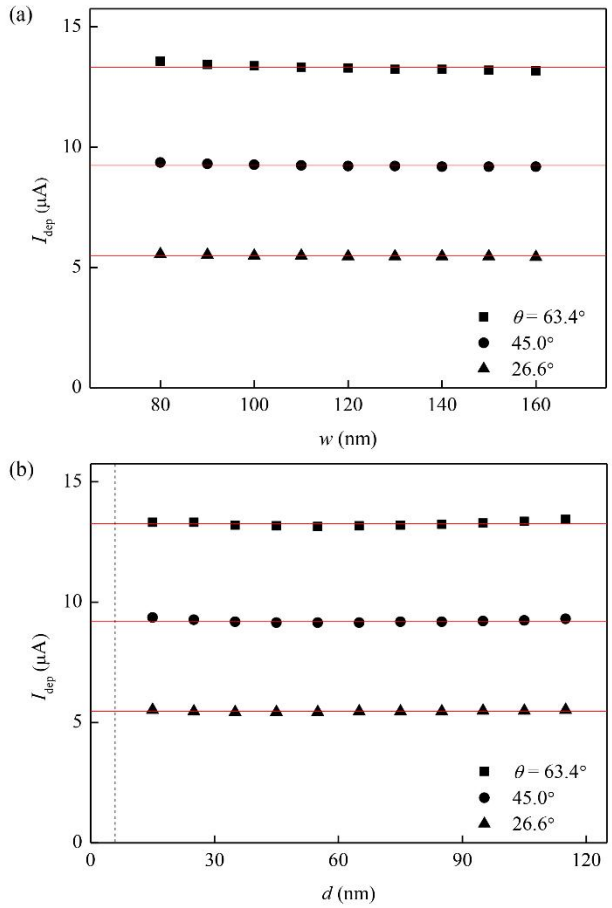

Figure 5.2 Plots of depinning current I_{dep} with respect to **a**, w (d =40 nm) and **b**, d (w =160 nm), for three different θ values denoted in the inset. The red lines show the average values of I_{dep} for each θ. The vertical dashed line indicates the DW width that I_{dep} starts to decrease to 0.

decreases drastically to 0 when d becomes smaller than the DW width (~ 6 nm). However, above this regime, I_{dep} is unchanged irrespective of d. This observation contradicts the intuitive expectations that a deeper notch will result in a larger pinning strength and also that a wider wire will require larger I_{dep} to keep the same current density through the wire.

To understand these unexpected observations, an analytic model

based on the geometric shape of the DW is considered. According to Ref. 73, the equilibrium DW geometry can be obtained by applying the variational principle for the energy-minimum state. The result states that a DW forms a circular arc with perpendicular intersections to the structural boundaries, as in Fig. 5.1. For the case that a uniform out-of-plane magnetic field H is applied to the DW, the radius R of the circular arc is given by the function of H as $R = \sigma_{\mathrm{DW}}/2M_{\mathrm{S}}H - \pi\lambda/2$, where σ_{DW} is the DW energy density, M_{S} is the saturation magnetization, and λ is the DW width [73].

The longitudinal SOT also generates an effective out-of-plane magnetic field H_{eff} on the DW. Recent studies have shown that H_{eff} is linearly proportional to the current density on the DW and thus, one can write $H_{\mathrm{eff}} = \varepsilon_{\mathrm{L}}J^*$ where J^* is the local current density perpendicular to the DW and ε_{L} is the current-to-field SOT efficiency [86,87]. Since the numerical calculation results revealed that J^* did not vary much throughout the DW, we first assumed the case of a constant H_{eff} $(= \varepsilon_{\mathrm{L}}\bar{J}^*)$ over the DW, where $\bar{J}^*$ denotes the average current density over the circular DW arc. The effect from the spatial variation of J^* will be discussed later. Then, by replacing the uniform H by H_{eff}, the above equation of R can be written as

$$R = \frac{\sigma_{\mathrm{DW}}}{2M_{\mathrm{S}}\varepsilon_{\mathrm{L}}\bar{J}^*} - \frac{\pi\lambda}{2} \tag{5.1}$$

Due to the inverse proportionality with respect to $\bar{J}^*$, R decreases as $\bar{J}^*$ increases. When R becomes smaller than the minimum

acceptable value R_{min} of the present notch geometry due to increasing current density $\bar{J}^*$, there is no longer a stable DW geometry and consequently, the DW is depinned from the notch [73]. Therefore the depinning threshold current density $\bar{J}^*_{\mathrm{dep}}$ can be written as

$$\bar{J}^*_{\mathrm{dep}} = \frac{\sigma_{\mathrm{DW}}}{2\varepsilon_{\mathrm{L}} M_{\mathrm{S}}} \frac{1}{R_{\mathrm{min}} + \pi\lambda/2}. \tag{5.2}$$

For the isosceles-triangular notches with an angle θ, the circular DW arc with the radius R_{min} which is on the verge of depinning, also has the opening angle θ, as can be seen in Fig. 5.1, since it has to make perpendicular intercepts both on the notch slope and the wire edge. Therefore, R_{min} has a simple geometric relation of $R_{\mathrm{min}} \sin\theta \cong h$, where h $(= w - d)$ is the gap distance of the notch. On a different note, the total depinning current I_{dep} across the DW satisfies a simple geometric relation of $I_{\mathrm{dep}} = \bar{J}^*_{\mathrm{dep}} R\theta t$, where $R\theta$ is the length of the circular DW arc. By combining these geometric relations to Eq. 5.2, one can finally obtain

$$I_{\mathrm{dep}} = \frac{\sigma_{\mathrm{DW}}\theta t}{2\varepsilon_{\mathrm{L}} M_{\mathrm{S}}} \left(1 + \frac{1}{2}\frac{\lambda}{h}\sin\theta\right)^{-1}. \tag{5.3}$$

Since h is much larger than λ (~a few nanometers) for practical notch geometry, one can simplify Eq. 5.3 into

$$I_{\mathrm{dep}} \cong \frac{\sigma_{\mathrm{DW}}\theta t}{2\varepsilon_{\mathrm{L}} M_{\mathrm{S}}}. \tag{5.4}$$

Eq. 5.3 and 5.4 clearly show that I_{dep} is insensitive to both w and d. This good conformity between the simulation results and the

analytic solution validates the present analytic model.

Figure 5.3a plots the simulation results of I_{dep} with respect to θ for three different D values. The plot clearly confirms the analytic prediction of Eq. 5.3 that I_{dep} has the linear proportionality on θ for each given D. Additionally, the slope α ($\equiv \partial I_{\mathrm{dep}}/\partial\theta$) of each curve is directly proportional to σ_{DW}, which varies with respect to D. According to Ref. 87, σ_{DW} of a Néel-type DW is given by

$$\sigma_{\mathrm{DW}} = \sigma_0 + 2K_{\mathrm{D}}\lambda - \pi|D| \quad \text{for } |D| > 4K_{\mathrm{D}}\lambda/\pi, \tag{5.5}$$

where K_{D} is the DW-anisotropy energy density and σ_0 is the Bloch-type DW energy density. By injecting I across the present DW configuration, the longitudinal SOT generates the effective magnetic field with the efficiency,

$$\varepsilon_{\mathrm{L}} = \frac{\pi}{2}\beta_{\mathrm{L}} \cos\psi. \tag{5.6}$$

Here, ψ is defined as the azimuthal angle of the magnetization, with 0 as the value of the Néel-type DW. Note that β_{L} is defined as the SOT efficiency for uniform magnetization, whereas ε_{L} is defined as the average SOT efficiency averaged over the DW profile. The constant $\pi/2$ comes from the integration over the DW profile. By organizing all the relations so far, one can rewrite Eq. 5.4 as

$$I_{\mathrm{dep}} \cong \frac{\sigma_0 + 2K_{\mathrm{D}}\lambda - \pi|D|}{\pi\beta_{\mathrm{L}}M_{\mathrm{S}}}\theta t \quad \text{for } |D| > 4K_{\mathrm{D}}\lambda/\pi. \tag{5.7}$$

The solid lines for each curve in Fig. 5.3a show the evaluation

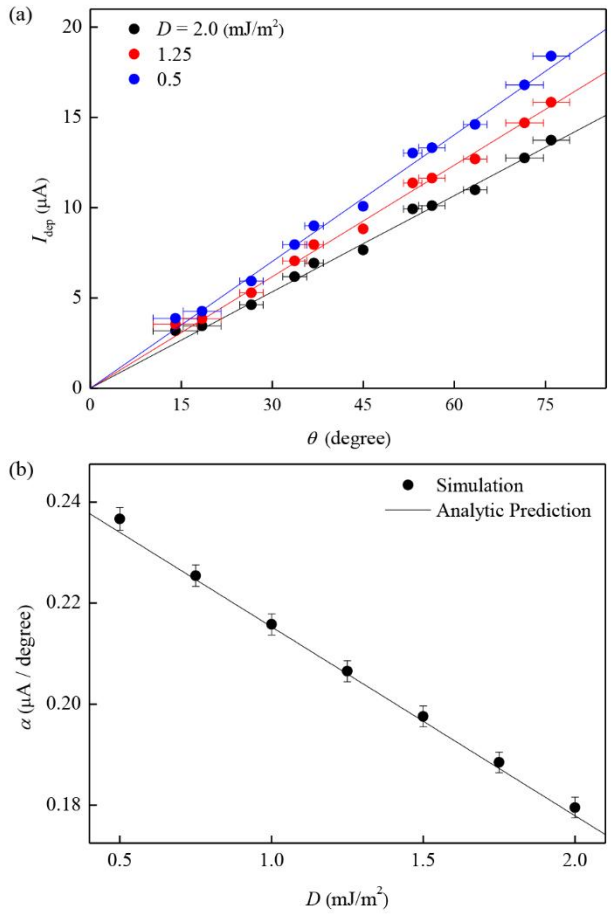

Figure 5.3 Comparison between analytic equation and the micromagnetic simulation. a, Plot of I_{dep} with respect to θ for several different D as denoted inside the plot with d (=40 nm) and w (=120 nm). The error bars in the abscissa axis show the maximum angle uncertainty from a digitized triangle. The lines show the best linear fitting for each D. **b**, Plot of α with respect to D. The error bars in the ordinate axis are the chi-square errors for the best linear fitting. The line shows the analytic prediction from Eq. 5.7.

of Eq. 5.7. Figure 5.3b plots α with respect to D obtained by the simulation (symbols) and the analytic equation (line). Again, the good conformity between the simulation and analytic results verifies the validity of the present model. This clear dependence on θ and D

provides a simple and useful guideline for designing a notched structure.

5.1.2 1st-order approximation for transverse spin-orbit torque

The effect of the transverse SOT is examined here. The transverse SOT generates an in-plane effective magnetic field transverse to the direction of the current. Such in-plane magnetic field consequently tilts the angle of the magnetization inside the DW. Since the full analytic solution including the transverse SOT is too complicated, we focus here only on the case of a large D, which is also desirable for practical applications. By treating the transverse SOT as perturbation on the DW magnetization angle from the Néel-type DW configuration, the 1st-order perturbed solution shows that the tilting angle $\delta\psi$ becomes $\delta\psi \cong \pi\lambda M_S \beta_T \bar{J}^* / (\pi D - 4K_D\lambda)$, where $\beta_T \bar{J}^*$ corresponds to the strength of the in-plane effective magnetic field due to the transverse SOT. Then, combining the ψ dependence of ε_L on Eq. 5.6, the depinning current I_{dep} can be rewritten as

$$I_{dep} \cong I_{dep}^0 \left[1 + \frac{1}{2}(\delta\psi)^2\right] = I_{dep}^0 \left[1 + \frac{1}{2}\left(\frac{\pi\lambda M_S \sin\theta}{(\pi D - 4K_D\lambda)h\theta t}\right)^2 \left(\beta_T I_{dep}^0\right)^2\right], \quad (5.8)$$

where I_{dep}^0 denotes the depinning current without the transverse SOT.

Figure 5.4 plots I_{dep} with respect to β_T (black) and β_L (blue), respectively. The figure clearly shows that I_{dep} is less sensitive to β_T in comparison to β_L. The 1st-order perturbative solution (black line) with respect to β_T matches well with the simulation results within 5% for the

range of β_T/β_L < 0.6. Since the overall dependence of I_{dep} on β_T is almost negligible (about 20% maximum over the broad simulation range) in comparison to that (about 2.5 times) of β_L, it would be practically sufficient to use Eq. 5.7 without detailed consideration of the transverse SOT.

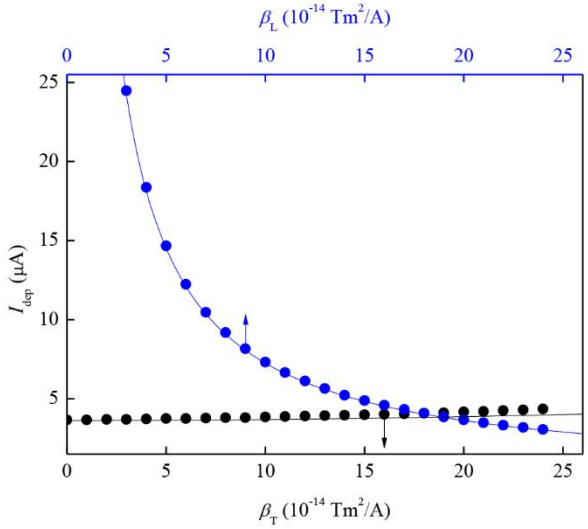

Figure 5.4 Plot of I_{dep} with respect to β_L (blue) and β_T (black), with *d* (=40 nm) and *w* (=120 nm). The symbols and lines represent the simulation results and the analytic predictions, respectively.

Finally, we discuss the possible errors that might affect the analysis. Although the local current density J^* has non-uniform distribution in both the magnitude and the direction near the notch tip, we assumed the uniform $\bar{J}^*$ normal to the DW. The calculation based on the register network reveals that there exists typically about 10% and 15-degree maximum of an error in the magnitude and the direction respectively, depending on the notch geometry. Such non-uniform J^* distribution can be the possible origin of the discrepancy between the

simulation and the analytic equation. However, note that the I_{dep} discrepancy does not exceed 5%. The digitization error of the notch slope based on square simulation cells also results in the uncertainty (about 5 degrees in maximum) of the notch angle, as in the error bars of Fig. 5.3a. Moreover, the structural imperfection of the wire and the notch in practical devices as well as the local temperature rise due to J^* will evidently affect I_{dep}, but such effects are beyond the scope of the present study.

We provided here an analytic equation of the SOT-driven depinning current from a triangular notch, whose validity was verified by micromagnetic simulation. Interestingly, the results revealed that the depinning current did not depend on the notch depth and the wire width, but was determined solely by the notch angle, the DMI strength, and the SOT efficiency. Such simple formula can provide a useful design rule for practical notch geometry, free from the notch depth and wire width.

5.2 1st-order equation of equilibrium angle under spin-orbit torque from any initial angle.

As frequently mentioned before, the spin-orbit torque is the essential main ingredient of the spintronics. However, the origin and the detailed recipe of the SOT still remains unclear. To resolve these uncertainties and fully understand the SOT, one should fundamentally measure a lot of spin-orbit torques from multiple systems.

The related measurement scheme is usually executed by measuring the tilting angle of a uniform magnetization induced by the SOT. Mostly, this is done electrically via the anomalous Hall effect or optically via the magneto optical Kerr effect (MOKE) [88]. Both schemes obtain the z component of a tilted magnetization (m_z) in the process. However, when the magnetization is perpendicular to the film plane at zero external magnetic field, the rate of change on m_z is too small to detect reliable signal. (usually, the SOT induced magnetization tilting is rather small). Therefore, it is preferable that the measurement is executed under an external in-plane magnetic field that tilts the magnetization first. In addition, since the Rashba scheme predicts an angle dependence of the SOT unlike the SHE scheme, measuring the SOT at varying initial tilting angle might be able to tell the still unknown origin of the SOT.

However, the analytic solution of the tilting angle with both external magnetic field and SOT is too complicated. The special 1st order solution at zero magnetic field is commonly utilized to measure the SOT [83]. To measure the SOT at non-zero magnetic field, a similar analytic solution should be derived. Here we present the 1st-order analytic solution of the magnetization angle under both the external magnetic field and the SOT. The LLG equation in Eq. 1.2 is revisited here.

$$\frac{\mathrm{d}\hat{m}}{\mathrm{d}t} = -\gamma_0 \hat{m} \times \vec{H}_{\mathrm{eff}} + \alpha \hat{m} \times \frac{\mathrm{d}\hat{m}}{\mathrm{d}t} - \beta_{\mathrm{L}} \hat{m} \times \left(\hat{m} \times \hat{m}_p\right) - \beta_{\mathrm{T}} \hat{m} \times \hat{m}_p \quad (5.9)$$

Since we measure the equilibrium angle under the magnetic field

and the SOT, $\frac{\mathrm{d}\hat{m}}{\mathrm{d}t}$ is zero here which leads to the Eq. 5.10,

$$0 = -\gamma_0 \hat{m} \times \vec{H}_{\mathrm{eff}} - \beta_{\mathrm{L}} \hat{m} \times \left(\hat{m} \times \hat{m}_p\right) - \beta_{\mathrm{T}} \hat{m} \times \hat{m}_p, \quad (5.10)$$

$$\text{with, } \vec{H}_{\mathrm{eff}} = \vec{H}_{\mathrm{ext}} + \vec{H}_{\mathrm{k}} = \vec{H}_{\mathrm{ext}} + H_{\mathrm{k}} \cos\theta \, \hat{z} \quad (5.11)$$

where the $\vec{H}_{\mathrm{ext}}$ is the external magnetic field vector and $\vec{H}_{\mathrm{k}}$ is the anisotropy field vector. The xyz-coordinate is oriented with the x axis along the current flow direction and the z axis along the film normal. The θ is the angle of $\hat{m}$ from the associated spherical coordinate. Note here that the spin-polarized direction of the SOT, $\hat{m}_p = \hat{y}$ in this orientation.

We have to solve the Eq. 5.10 and obtain the equilibrium $\hat{m}$ (θ and φ). Since the pure analytic solution is not obtainable, the solution is derived in 2 separate steps. Frist, we solve the Eq. 5.10 under the zero SOT. With this angle fixed as the initial angle, the 1st-order perturbed angle under spin-orbit torque is approximated, assuming the angle deviation by the SOT is small enough.

Beforehand, we use the spherical coordinate system to expand the vector equations in Eq. 5.10 to two separate scalar equations of θ and φ.

$$(H_{\mathrm{x}} \cos\varphi + H_{\mathrm{y}} \sin\varphi) \cos\theta - H_{\mathrm{z}} \sin\theta - H_{\mathrm{k}} \cos\theta \sin\theta +$$

$$H_{\mathrm{L}} \cos\varphi + H_{\mathrm{T}} \cos\theta \sin\varphi = 0, \quad (5.12)$$

$$-H_{\mathrm{x}} \sin\varphi + H_{\mathrm{y}} \cos\varphi - H_{\mathrm{L}} \cos\theta \sin\varphi + H_{\mathrm{T}} \cos\varphi = 0. \quad (5.13)$$

The $H_{\mathrm{x,y,z}}$ is the respective xyz components of $\vec{H}_{\mathrm{ext}}$. The $H_{\mathrm{L,T}}$ represents the associated magnetic field induced by the $\beta_{\mathrm{L,T}}$ terms of the SOT.

As stated above, we first solve the special case of $H_{\mathrm{L,T}} = 0$ that is, (this initial angle will be denoted with 0 subscripts)

$$(H_{\mathrm{x}} \cos\varphi_0 + H_{\mathrm{y}} \sin\varphi_0) \cos\theta_0 - H_{\mathrm{z}} \sin\theta_0 - H_{\mathrm{k}} \cos\theta_0 \sin\theta_0 = 0 \quad , \quad (5.14)$$

$$-H_{\mathrm{x}} \sin\varphi_0 + H_{\mathrm{y}} \cos\varphi_0 = 0. \quad (5.15)$$

which leads to,

$$H_{\mathrm{in}} \cos\theta_0 - H_{\mathrm{z}} \sin\theta_0 - H_{\mathrm{k}} \cos\theta_0 \sin\theta_0 = 0, \quad (5.16)$$

$$\varphi_0 = \varphi_{\mathrm{field}}. \quad (5.17)$$

For zero SOT, the azimuthal angle of the magnetization becomes the azimuthal angle of the external magnetic field (φ_{field}). With the H_{in} as the in-plane component of the external magnetic field, we can solve the Eq. 5.16 which is the 4$^{\mathrm{th}}$-order polynomial of the $\cos\theta_0$, to obtain the initial tilting angle by the magnetic field.

Then, by using the Eq. 5.18 to 5.21, assuming small deviation by the SOT,

$$\cos\theta = \cos(\theta_0 + d\theta) \cong \cos\theta_0 - \sin\theta_0 \, d\theta, \quad (5.18)$$

$$\cos\varphi = \cos(\varphi_0 + d\varphi) \cong \cos\varphi_0 - \sin\varphi_0\, d\varphi, \tag{5.19}$$

$$\sin\theta = \sin(\theta_0 + d\theta) \cong \sin\theta_0 + \cos\theta_0\, d\theta, \tag{5.20}$$

$$\sin\varphi = \sin(\varphi_0 + d\varphi) \cong \sin\varphi_0 + \cos\varphi_0\, d\varphi. \tag{5.21}$$

the 1st-order solution of the Eq. 5.12 and 5.13 can be obtained. In addition to the assumption $d\theta, d\varphi \ll 1$, the $H_{\mathrm{L,T}} \ll H_{\mathrm{k}}$ was also assumed in the same context that the SOT is small. The derived solution is the Eq. 5.22 and 5.23.

$$d\theta \cong \frac{H_{\mathrm{T}}Cos\theta_0 Sin\varphi_0 + H_{\mathrm{L}}Cos\varphi_0}{(H_{\mathrm{in}}Sin\theta_0 + H_{\mathrm{z}}Cos\theta_0 + H_{\mathrm{k}}Cos2\theta_0)}, \tag{5.22}$$

$$d\varphi \cong \frac{1}{H_{\mathrm{in}}}(H_T Cos\varphi_0 - H_L Cos\theta_0 Sin\varphi_0). \tag{5.23}$$

With these 1st-order analytic equations, one can measure the SOT at any initial angle induced by the magnetic field. This not only improves the SOT signal by enabling the measurement at tilted angle, but also enables the measurement of the angular dependence of the SOT that can eventually lead to shedding a light on the origin of the SOT. This technique is being utilized in the according measurement setups by fellow researchers, J. S. Kim and J. H. Park.

5.3 Optical measurement of magnetic anisotropy field in nanostructured-ferromagnetic thin films

The magnetic anisotropy field plays a crucial and basic role in

all the spin dynamics stated so far. Here, we propose a magnetometric technique to measure the magnetic anisotropy field in nanostructured ferromagnetic thin films. This technique utilizes a magneto-optical-Kerr-effect microscope equipped with two-axis electromagnets. By measuring the out-of-plane hysteresis loops and analyzing their saturated magnetization with respect to the in-plane magnetic field, the magnetic anisotropy field is uniquely quantified within the scheme of the Stoner-Wohlfarth theory. The present technique can be applied to small nanostructures, enabling in-situ determination of the magnetic anisotropy field of nanoscale-devices.

Magnetic domain-wall memory devices [89] have attracted a great deal of attention as potential candidates of emerging memory devices. Of such devices, the most common is nanostructured ferromagnetic thin films with perpendicular magnetic anisotropy (PMA) [90]. The effective field induced by the PMA — namely, the magnetic anisotropy field — has been found to play an important role in the magnetization dynamics driven by the spin-orbit torque (SOT) [91-94]. Therefore, precise measurement of the magnetic anisotropy field is essential to understand the SOT-induced magnetization dynamics as well as to quantify the magnitude of the SOT. To measure such magnetic anisotropy fields, torque magnetometry [95] has been the conventional technique for bulk materials, but this technique is not applicable to nanostructured devices due to their small volume and consequently weak signal. Recently, magnetometry based on the extraordinary Hall effect (EHE) has been proposed to measure the magnetic anisotropy field from

ferromagnetic thin films [96]. However, this technique requires specific measurement geometry to inject the electric current into the structure, and exhibits a number of artifacts that require sophisticated and time-consuming analysis techniques. Here, we propose another magnetometric technique based on optical measurement which allows the magnetic anisotropy field to be measured from nanostructured devices without any modification on specific geometry.

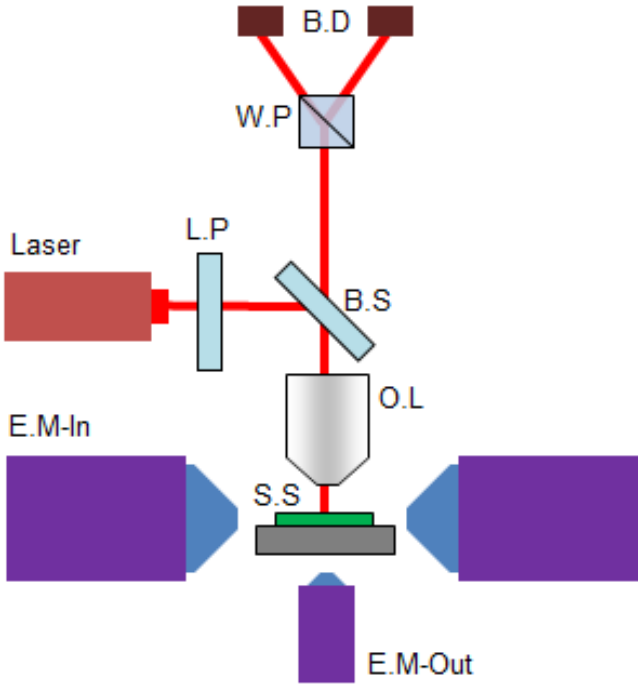

Figure 5.5 Schematics of the MOKE setup. E.M-In/Out is the in-plane/out-of-plane electromagnet. S.S refers to the sample stage, O.L refers to the objective lens, B.S refers to the beam splitter, and L.P refers to the linear polarizer. W.P refers to the Wollaston prism and B.D. refers to the balanced detector.

Figure 5.5 shows a schematic diagram of the measurement setup. The magnetic signal from the sample is measured by a magneto-optical-Kerr-effect (MOKE) microscope with a spatial resolution better than 3

μm and an objective lens with a numerical aperture (=0.45) [97,98]. This microscope is equipped with two electromagnets to apply the in-plane and out-of-plane magnetic fields up to 600 mT and 150 mT, respectively.

The ferromagnetic Pd/Co/Pt films were measured. All the films exhibit PMA. The detailed sample structure is 5.0-nm Ta/1.8-nm Pd/0.3-nm Co/2.5-nm Pt, which was prepared on a Si substrate with a 100-nm-thick SiO2 layer by dc magnetron sputtering. For the measurement of the magnetic anisotropy field, an in-plane magnetic field bias H_{in} was applied to the sample, and the out-of-plane magnetic hysteresis loop was then measured by sweeping the out-of-plane magnetic field H_{out}. Figure 5.6 shows the magnetic hysteresis loops measured under various in-plane field biases H_{in}. The figure clearly shows that the shape of the hysteresis loops is sensitive to the strength of H_{in}.

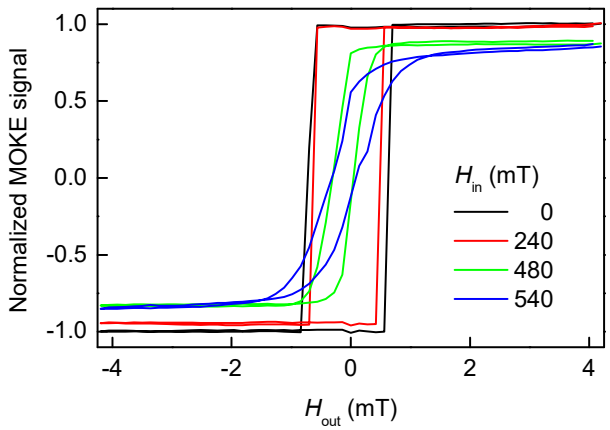

Figure 5.6 Out-of-plane magnetic hysteresis loops for various H_{in} denoted inside the figure. The ordinate is the MOKE signal normalized by the saturated magnetization measured from the hysteresis loop with $H_{\text{in}} = 0$.

The variation of the hysteresis loops can be explained within the context of the Stoner-Wohlfarth theory, in which the magnetic energy E is given by $E = K_{\mathrm{U}} \sin^2\theta - M_{\mathrm{S}} H \cos(\theta - \varphi)$, where K_{U} is the uniaxial magnetic anisotropy constant with the out-of-plane easy axis, M_{S} is the saturation magnetization and H is the strength of the external magnetic field. Here, the angle θ of the magnetization and the angle φ of the external magnetic field are defined as the polar angles with respect to the easy axis. The magnetic anisotropy field H_{K} is then defined as $H_{\mathrm{K}} = 2K_{\mathrm{U}}/M_{\mathrm{S}}$ [99,100]. Since the present experimental geometry gives $H_{\mathrm{in}} = H \sin\varphi$ and $H_{\mathrm{out}} = H \cos\varphi$, the magnetic energy can be written as

$$E = \frac{M_{\mathrm{S}} H_{\mathrm{K}}}{2} \sin^2\theta - M_{\mathrm{S}} H_{\mathrm{out}} \cos\theta - M_{\mathrm{S}} H_{\mathrm{in}} \sin\theta. \quad (5.24)$$

The equilibrium angle θ_{eq} is then obtained by the energy minimization condition i.e.

$$\left.\frac{\partial E}{\partial \theta}\right|_{\theta_{\mathrm{eq}}} = M_{\mathrm{S}} H_{\mathrm{K}} \sin\theta_{\mathrm{eq}} \cos\theta_{\mathrm{eq}} + M_{\mathrm{S}} H_{\mathrm{out}} \sin\theta_{\mathrm{eq}} - M_{\mathrm{S}} H_{\mathrm{in}} \cos\theta_{\mathrm{eq}} = 0 \quad . \quad (5.25)$$

The exact solution of Eq. 5.25 is fairly complicated. However, two special cases exist with simple solutions, which consequently provide two distinct measurement schemes.

The first scheme (Scheme I) is based on the saturated θ_{eq} measured under a H_{out} larger than the coercive field. For this case, one can easily obtain the solution as $\theta_{\mathrm{eq}} = M_{\mathrm{S}} H_{\mathrm{in}} / (M_{\mathrm{S}} H_{\mathrm{K}} + M_{\mathrm{S}} H_{\mathrm{out}})$ or

$$\cos\theta_{eq} \cong 1 - \frac{1}{2}\frac{H_{in}^2}{(H_K + H_{out})^2}, \quad (5.26)$$

for a small θ_{eq}. Note that $\cos\theta_{eq}$ can be easily measured experimentally from the normalized magnetic hysteresis loops in the Fig. 5.6. Figure 5.7a shows the plot of $\cos\theta_{eq}$ with respect to H_{in}, measured for H_{out}=4 mT. It is clear from the figure that the measured $\cos\theta_{eq}$ (H_{in}) follows the behavior predicted by Eq. 5.26. The red line shows the best fit with Eq. 5.26, which quantifies H_K as 1013±50 mT.

The second scheme (Scheme II) is proposed to analyze H_K based on the measurement of the remnant $\cos\theta_{eq}$ with $H_{out} = 0$ [101]. For this case, Eq. 5.25 can be simplified to $M_S H_K \sin\theta_{eq}\cos\theta_{eq} - M_S H_{in}\cos\theta_{eq} = 0$, providing the solutions $\sin\theta_{eq} = H_{in}/H_K$ and $\cos\theta_{eq} = 0$. Since the latter solution is found to be unstable, the unique stable solution consequently provides the relation,

$$\cos\theta_{eq} = \sqrt{1 - (H_{in}/H_K)^2}. \quad (5.27)$$

However, we found that this method fails to quantify H_K. The symbols in Fig. 5.7b show the measured $\cos\theta_{eq}$ with respect to H_{in}. The blue dashed lines show the curves of Eq. 5.27 with different values of H_K as denoted inside the plot. It is clear from the figure that none of the curves of Eq. 5.27 fit the experimental data. The failure is possibly caused by either the multi-domain formation or the large variation of the magnetization direction due to the irregularities in the anisotropy at the remnant states. The best fitting value for small H_{in} (< 300 mT) is similar

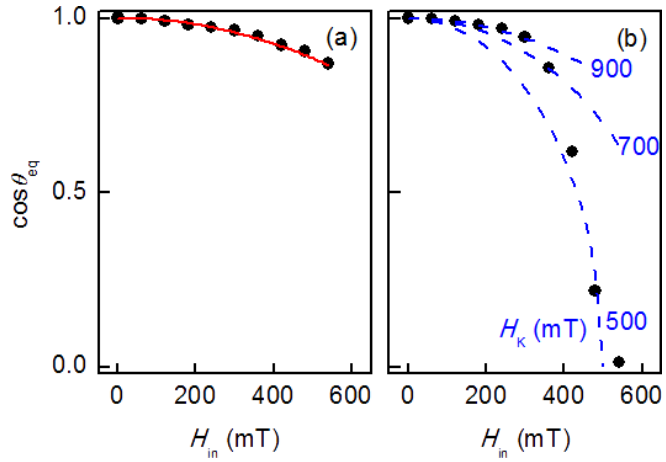

Figure 5.7 Plots of a, the saturated $\cos\theta_{eq}$ with H_{out}=4 mT and b, the remnant $\cos\theta_{eq}$ with H_{out}=0 mT, measured with respect to various H_{in}. The red solid line in a shows the best fits with Eq. 5.26. The blue dashed lines in b show the curves of Eq. 5.27 with several different H_K as denoted inside the plot.

to that obtained by Scheme I, but the best fitting value for all the data occurs when H_K is about 500 mT, which considerably differs to that obtained by Scheme I.

To examine the validity of the value obtained by Scheme I, we compare it with the value measured by the electrical method based on the EHE measurement [96]. Due to the sizeable ordinary and planar Hall effects observed in these samples, the electrical measurement is accompanied with sizeable artifacts caused by the ordinary and planar Hall effects. By measuring these artifacts from their different angular dependence between the magnetic field and the magnetization directions, the best estimation of H_K is found to be 952±62 mT, which is accordant with the value determined by Scheme I within the experimental accuracy. One can therefore conclude that Scheme I (rather than Scheme II)

provides better accuracy in the H_K measurement. It is also worth noting that the present optical scheme provides an easier way to analyze H_K compared to the electrical method that requires sophisticated analysis of the artifacts, including the ordinary and planar Hall effect.

In conclusion, we propose an optical magnetometric technique by using a MOKE microscope equipped with two electromagnets. By measuring the out-of-plane hysteresis loops under various in-plane magnetic field biases, the magnetic anisotropy field is quantified based on the Stoner-Wohlfarth theory of the magnetization rotation. Due to the nature of the optical measurement scheme, the present technique can be applied to a local spot of nanostructured devices, enabling a versatile diagnosis on actual devices.

Chapter 6. Conclusion

In this thesis, we have mainly investigated the possible application of spintronic devices via micromagnetic simulation. Although the spintronic device is being extensively studied to become next-generation logic and memory device, there are still a lot of small and large obstacles for the field to overcome. While this can be solved via various methodologies, we focused on contemplating fresh ideas through micromagnetic simulations and analytic equations.

Among various possible application ideas presented here, the spin-Hall effect modulation is soundly the highlight of the thesis due to its rich behavior and design capability. For instance, the new reliable DW pinning/depinning mechanisms at the spin-Hall-effect-modulation boundary was proposed and explained. Furthermore, it was especially surprising that a skyrmion rotated around a tilted spin-Hall-effect-modulation boundary, which eventually led to the introduction of a whole new concept of spin-torque oscillator that can overcome troubling issues of conventional spin-torque oscillators.

Moreover, the application of spintronics to the rising field of neuromorphic engineering is also investigated. Notably, the power-efficient synapse and neuron device can both be achieved by DW motion with a magnetic tunnel junction. As the field is rather fresh, all the exploding new ideas including the ones presented here are valuable on its own. In addition, this thesis also investigates the possible analytic equations that are used to design a device or to measure a magnetic

parameter based on associated models.

By travelling though these ideas that utilize the exotic behaviors in nano-scale systems with broken symmetries, not only the application possibilities but also the physical understanding can be heightened. Ironically in recent physics, the interesting phenomena come from breaking the symmetries via various constraints rather than investigating them. Since most symmetric and consequently global properties are rather easily and already explained, the constraints are more valid elements that define a specific system. Hence, introducing new constraints and investigating them now directly relates to discovering a new academic field of physics. The ‘color’ of a jewel comes from the impurities within, not from the crystalline symmetry. Contemplating these colors of a jewel, or the new ideas of case-dependent constraints will eventually lead to the discovery of new physics. This thesis and the years spent was thus dedicated on meeting fresh ideas and playing, even dancing with them.

References

1. M. N. Baibich *et al.* Giant Magnetoresistance of (001)Fe/(001)Cr Magnetic Superlattices. *Phys. Rev. Lett.* **61**, 2472 (1988).

2. J. C. Slonczewski, Current-driven excitation of magnetic multilayers. *J. Magn. Magn. Mater.* **159**, L1–L7 (1996).

3. L. Berger, Emission of spin waves by a magnetic multilayer traversed by a current. *Phys. Rev. B* **54**, 9353–9358 (1996).

4. M. Tsoi *et al.* Excitation of a magnetic multilayer by an electric current. *Phys. Rev. Lett.* **80**, 4281–4284 (1998).

5. E. B. Myers *et al.* Current-induced switching of domains in magnetic multilayer devices. *Science* **285**, 867–870 (1999).

6. J. A. Katine *et al.* Current-driven magnetization reversal and spin-wave excitations in Co/Cu/Co pillars. *Phys. Rev. Lett.* **84**, 3149–3152 (2000).

7. A. Thiaville *et al.* Micromagnetic understanding of current-driven domain wall motion in patterned nanowires. *Europhys. Lett.* **69**, 990 (2005).

8. D. Chiba *et al.* Control of multiple magnetic domain walls by current in a Co/Ni nano-wire. *Appl. Phys. Express* **3**, 073004 (2010).

9. T. Koyama *et al.* Observation of the intrinsic pinning of a magnetic domain wall in a ferromagnetic nanowire. *Nature Mater.* **10**, 194 (2011).

10. K. Ueda *et al.* Temperature dependence of carrier spin polarization

determined from current-induced domain wall motion in a Co/Ni nanowire. *Appl. Phys. Lett.* **100**, 202407 (2012).

11. G. Tatara *et al.* Theory of current-driven domain wall motion: Spin transfer versus momentum transfer. *Phys. Rev. Lett.* **92**, 086601 (2004).

12. S. Zhang *et al*. Roles of nonequilibrium conduction electrons on the magnetization dynamics of ferromagnets. *Phys. Rev. Lett.* **93**, 127204 (2004).

13. A. Mougin *et al.* Domain wall mobility, stability and Walker breakdown in magnetic nanowires. *Europhys. Lett.* **78**, 5 (2007).

14. K.-J. Kim *et al*. Electric control of multiple domain walls in Pt/Co/Pt nanotracks with perpendicular magnetic anisotropy. *Appl. Phys. Express* **3**, 083001 (2010).

15. T. A. Moore *et al*. High domain wall velocities induced by current in ultrathin Pt/Co/AlO_x wires with perpendicular magnetic anisotropy. *Appl. Phys. Lett.* **93**, 262504 (2008).

16. I. M. Miron *et al*. Fast current-induced domain-wall motion controlled by the Rashba effect. *Nature Mater.* **10**, 419-423 (2011).

17. J.-C. Lee *et al*. Universality classes of magnetic domain wall motion. *Phys. Rev. Lett.* **107**, 067201 (2011).

18. L. Liu *et al.* Current-induced switching of perpendicularly magnetized magnetic layers using spin torque from the spin Hall effect. *Phys. Rev. Lett.* **109**, 096602 (2012).

19. L. Liu *et al.* Spin-Torque Switching with the Giant Spin Hall Effect

of Tantalum. *Science* **336**, 555 (2012).

20. S.-M. Seo *et al.* Current-induced motion of a transverse magnetic domain wall in the presence of spin Hall effect. *Appl. Phys. Lett.* **101**, 022405 (2012).

21. I. M. Miron *et al.* Current-driven spin torque induced by the Rashba effect in a ferromagnetic metal layer. *Nat. Mater.* **9**, 230 (2010).

22. I. M. Miron *et al.* Perpendicular switching of a single ferromagnetic layer induced by in-plane current injection. *Nature* **476**, 189 (2011).

23. U. H. Pi *et al.* Tilting of the spin orientation induced by Rashba effect in ferromagnetic metal layer. *Appl. Phys. Lett.* **97**, 162507 (2010).

24. T. Suzuki *et al.* Current-induced effective field in perpendicularly magnetized Ta/CoFeB/MgO wire. *Appl. Phys. Lett.* **98**, 142505 (2011).

25. K.-W. Kim *et al.* Magnetization dynamics induced by in-plane currents in ultrathin magnetic nanostructures with Rashba spin-orbit coupling. *Phys. Rev. B* **85**, 180404(R) (2012).

26. L. Liu *et al.* Spin-torque ferromagnetic resonance induced by the spin Hall effect. *Phys. Rev. Lett* **106**, 036601 (2011).

27. P. P. J. Haazen *et al.* Domain wall depinning governed by the spin Hall effect. *Nat. Mater* **12**, 299-303 (2013).

28. A. Thiaville *et al.* Dynamics of Dzyaloshinskii domain walls in ultrathin magnetic films. *Europhys. Lett.* **100**, 57002 (2012).

29. I. E. Dzialoshinskii, Thermodynamic theory of weak ferromagnetism in antiferromagnetic substances. *Sov. Phys. JETP* **5**, 1259–1262

(1957).

30. T. Moriya, Anisotropic superexchange interaction and weak ferromagnetism. *Phys. Rev.* **120**, 91–98 (1960).

31. A. Fert *et al.* Role of anisotropic exchange interactions in determining the properties of spin-Glasses. *Phys. Rev. Lett.* **44**, 1538 (1980).

32. S. Heinze *et al.* Spontaneous atomic-scale magnetic skyrmion lattice in two dimensions. *Nat. Phys.* **7**, 713 (2011).

33. X. Z. Yu *et al.* Real-space observation of a two-dimensional skyrmion crystal. *Nature* **465**, 901-904 (2010).

34. A. Bogdanov *et al.* Thermodynamically stable magnetic vortex states in magnetic crystals. *J. Magn. Magn. Mater.* **138**, 255 (1994).

35. U. K. Roßler *et al.* Spontaneous skyrmion ground states in magnetic metals. *Nature* **442**, 797-801 (2006).

36. N. Romming *et al.* Writing and deleting single magnetic skyrmions. *Science* **341**, 636-639 (2013).

37. J. Sampaio *et al.* Nucleation, stability and current-induced motion of isolated magnetic skyrmions in nanostructures. *Nat. Nanotechnol.* **8**, 839 -844 (2013).

38. S. Rohart *et al.* Skyrmion confinement in ultrathin film nanostructures in the presence of Dzyaloshinskii-Moriya interaction *Phys. Rev. Lett. B* **88**, 184422 (2013).

39. S. H. Yang *et al.* Domain-wall velocities of up to 750 m s^{-1} driven by exchange-coupling torque in synthetic antiferromagnets. *Nat. Nanotechnol* **10**, 221-226 (2015).

40. K. –J. Kim *et al.* Fast domain wall motion in the vicinity of the angular momentum compensation temperature of ferrimagnets. *Nat. Mater* **16**, 1187-1192 (2017).

41. L. Caretta *et al.* Fast current-driven domain walls and small skyrmions in a compensated ferrimagnet. *Nat. Nanotechnol* **13**, 1154-1160 (2018).

42. M. J. Donahue *et al.* OOMMF User's Guide, Version 1.0. Interagency Report NISTIR 6376 (National Institute of Standards and Technology, Gaithersburg, 1999).

43. S. S. P. Parkin *et al.* Magnetic domain-wall racetrack memory. *Science* **320**, 190-194 (2008).

44. S. I. Kiselev *et al.* Microwave oscillations of a nanomagnet driven by a spin–polarized current. *Nature* **425**, 380–383 (2003).

45. W. H Rippard *et al.* Direct–current induced dynamics in $Co_{90}Fe_{10}/Ni_{80}Fe_{20}$ point contacts. *Phys. Rev. Lett.* **92**, 27201 (2004).

46. I. N. Krivorotov *et al.* Time domain measurements of nanomagnet dynamics driven by spin–transfer torques. *Science* **307**, 228–231 (2005).

47. D. Houssameddine *et al.* Spin–torque oscillator using a perpendicular polarizer and a planar free layer. *Nature Mater*. **6**, 447–453 (2007).

48. A. A. Tulapurkar *et al.* Spin–torque diode effect in magnetic tunnel junctions. *Nature* **438**, 339–342 (2005).

49. P. K. Muduli *et al.* Nonlinear frequency and amplitude modulation of a nanocontact–based spin–torque oscillator. *Phys. Rev. B* **81**, 140408 (2010).

50. J. G. Zhu *et al.* Microwave assisted magnetic recording utilizing perpendicular spin torque oscillator with switchable perpendicular electrodes. *IEEE Trans. Magn.* **46**, 751–757 (2010).

51. R. L. Stamps *et al.* The 2014 magnetism roadmap. *J. Phys. D: Appl. Phys.* **47**, 333001 (2014).

52. S. Sani *et al.* Mutually synchronized bottom–up multi–nanocontact spin–torque oscillators. *Nat. Commun* **4**, 2731 (2013).

53. G. Khalsa *et al.* Critical current and linewidth reduction in spin–torque nano–oscillators by delayed self–injection. *Appl. Phys. Lett.* **106**, 242402 (2015).

54. V.S. Pribiag *et al.* Magnetic vortex oscillator driven by d.c. spin–polarized current. *Nat. Phys* **3**, 498–503 (2007).

55. T. Chen, *et al.* Spin–torque and spin–Hall nano–oscillators. *Proc. IEEE* **104**, 10 (2016).

56. F. Garcia–Sanchez *et al.* A skyrmion–based spin–torque nano–oscillator. *New J. Phys.* **18**, 075011 (2016).

57. S. Zhang *et al.* Current–induced magnetic skyrmions oscillator. *New J. Phys.* **17**, 023061 (2015).

58. J. E. Hirsch, Spin Hall Effect. *Phys. Rev. Lett* **83**, 9 (1999).

59. A. A. Thiele, Steady–state motion of magnetic domains. *Phys. Rev. Lett* **30**, 230–233 (1973).

60. W. Jiang *et al.* Direct observation of the skyrmion Hall effect. *Nat. Phys* **13**, 162–169 (2017).

61. A. A. Thiaville *et al.* Dynamics of Dzyaloshinskii domain walls in ultrathin magnetic films. *Europhys. Lett.* **100**, 57002 (2012).

62. J. Sampaio *et al.* A. Nucleation, stability and current–induced motion of isolated magnetic skyrmions in nanostructures. *Nat. Nanotechnol* **8**, 839–844 (2013).

63. X. Wang *et al.* Spintronic memristor through spin-torque-induced magnetization motion. *IEEE Electron Device Letters* **30**, 3 (2009).

64. Y. Huang *et al.* Magnetic skyrmion-based synaptic devices. *Nanotechnology* **28**, 8 (2017)

65. S. S. P. Parkin *et al.* Magnetic domain-wall racetrack memory. *Science* **320**, 190 (2008).

66. D. A. Allwood Magnetic domain-wall logic. *et al. Science* **309**, 1688 (2005).

67. J. Vogel *et al.* Direct observation of massless domain wall dynamics in nanostripes with perpendicular magnetic anisotropy. *Phys. Rev. Lett.* **108**, 247202 (2012).

68. T. Taniguchi *et al.* Precise control of magnetic domain wall displacement by a nanosecond current pulse in Co/Ni nanowires. *Appl. Phys. Express* **8**, 073008 (2015).

69. U. Bauer *et al.* Voltage-controlled domain wall traps in ferromagnetic

nanowires. *Nat. Nanotechnol* **8**, 411-416 (2013).

70. F. Cayssol *et al.* Domain wall creep in magnetic wires. *Phys. Rev. Lett.* **92**, 107202 (2004).

71. J. Wunderlich *et al.* Influence of geometry on domain wall propagation in a mesoscopic wire. *IEEE Trans. Magn.* **37**, 2104 (2001).

72. S.-B. Choe *et al.* Direct observation of Barkhausen effect in strip-patterned ferromagnetic Co/Pd multilayer film. *J. Appl. Phys.* **99**, 103902 (2006).

73. K.-J. Kim *et al.* Analytic theory of wall configuration and depinning mechanism in magnetic nanostructure with perpendicular magnetic anisotropy. *J. Magn. Magn. Mater.* **321**, 2197 (2009).

74. K.-S. Ryu *et al.* Chiral spin torque at magnetic domain walls. *Nat. Nanotechnol* **8**, 527 (2013).

75. P. P. J. Haazen *et al.* Domain wall depinning governed by the spin Hall effect. *Nat. Mater.* **12**, 299 (2013).

76. S. Emori *et al.* Current-driven dynamics of chiral ferromagnetic domain walls. *Nat. Mater.* **12**, 611-616 (2013).

77. S.-M. Seo1 *et al.* Current-induced motion of a transverse magnetic domain wall in the presence of spin Hall effect. *Appl. Phys. Lett.* **101**, 022405 (2012).

78. K.-W. Kim *et al.* Magnetization dynamics induced by in-plane currents in ultrathin magnetic nanostructures with Rashba spin-orbit coupling. *Phys. Rev. B* **85**, 180404(R) (2012).

79. A. V. Khvalkovskiy *et al.* Matching domain-wall configuration and spin-orbit torques for efficient domain-wall motion. *Phys. Rev. B* ***87***, 020402(R) (2013).

80. H. Fukushima *et al.* Volume average demagnetizing tensor of rectangular prisms. *IEEE Trans. Magn.* **34**, 193-198 (1998).

81. D.-H. Kim *et al.* Maximizing domain-wall speed via magnetic anisotropy adjustment in Pt/Co/Pt films. *Appl. Phys. Lett.* **104**, 142410 (2014).

82. P. J. Metaxas *et al.* Creep and Flow Regimes of Magnetic Domain-Wall Motion in Ultrathin Pt/Co/Pt Films with Perpendicular Anisotropy. *Phys. Rev. Lett.* **99**, 217208 (2007).

83. U.-H. Pi *et al.* Tilting of the spin orientation induced by Rashba effect in ferromagnetic metal layer. *Appl. Phys. Lett.* **97**, 162507 (2010).

84. D.-Y. Kim *et al.* Determination of magnetic domain-wall types using Dzyaloshinskii–Moriya-interaction-induced domain patterns. *Appl. Phys. Lett.* **106**, 262403 (2015).

85. M. J. Donahue *et al.* OOMMF User's Guide, Version 1.0. Interagency Report NISTIR 6376 (National Institute of Standards and Technology, Gaithersburg, 1999).

86. M. D. Stiles and J. Miltat, in Spin Dynamics in Confined Magnetic Structures III (Springer, Berlin, 2006) p. 225–308.

87. A. A, Thiaville *et al.* Dynamics of Dzyaloshinskii domain walls in ultrathin magnetic films. *Europhys. Lett.* **100**, 57002 (2012).

88. J. –S. Kim *et al.* Artifact-free optical spin-orbit torque magnetometry.

Appl. Phys. Lett. **114**, 182402 (2019).

89. S. S. P. Parkin *et al.* Magnetic domain-wall racetrack memory. *Science* **320**, 190 (2008).

90. I. M. Miron *et al*. Perpendicular switching of a single ferromagnetic layer induced by in-plane current injection. *Nature* **476**, 189-193 (2011).

91. K. Garello *et al*. Symmetry and magnitude of spin-orbit torques in ferromagnetic heterostructure. *Nat. Nanotech.* **8**, 587-593 (2013).

92. A.V. Khvalkovskiy *et al*. Matching domain-wall configuration and spin-orbit torques for efficient domain-wall motion. *Phys. Rev. B* **87**, 020402 (2013).

93. P. Gambardella *et al. Philosophical Transactions of the Royal Society A: Mathematical, Physical and Engineering Sciences* **369**, 3175-3197 (2011).

94. I. M. Miron *et al*. Current-driven spin torque induced by the Rashba effect in a ferromagnetic metal layer. *Nat. Mater.* **9**, 230-234 (2010).

95. W. H. Meiklejohn *et al.* New magnetic anisotropy. *Phys. Rev. Lett.* **102**, 1413 (1956).

96. K.W. Moon *et al*. Determination of perpendicular magnetic anisotropy in ultrathin ferromagnetic films by extraordinary Hall voltage measurement. *Rev. Sci. Instrum.* **80**, 113904 (2009).

97. K.J. Kim *et al*. Interdimensional universality of dynamic interfaces. *Nature* **458**, 740-742 (2009).

98. D.A. Allwood *et al*. Magneto-optical Kerr effect analysis of magnetic

nanostructures. *J. Phys. D: Appl. Phys.* **36**, 2175 (2003).

99. C. Tannous *et al.* The Stoner–Wohlfarth model of ferromagnetism. *Eur. J. Phys.* **29**, 475 (2008).

100. D. Jiles *et al.* Introduction to Magnetism and Magnetic Materials, Chapman & Hall, London (1998) pp. 370~375.

101. U. Bauer *et al.* Magneto-ionic control of interfacial magnetism. *Nat. Mater.* **14**, 174-181 (2015).

Publication List

1. Sang-Jun Yun, Joon Moon, **Hyun-Seok Whang**, and Sug-Bong Choe, 한국자기학회지 25, 1 (2015).

2. **Hyun-Seok Whang**, Sang-Jun Yun, Joon Moon, and Sug-Bong Choe, J. Magn 20, 1 (2015).

3. **Hyun-Seok Whang** and Sug-Bong Choe, Appl. Phys. Express 11, 043003 (2018).

4. Dae-Yun Kim, Min-Ho Park, Yong-Keun Park, Joo-Sung Kim, Yoon-Seok Nam, **Hyun-Seok Whang**, Duck-Ho Kim, Soong-Geun Je, Byoung-Chul Min, and Sug-Bong Choe, Phys. Rev. B 97, 134407 (2018).

5. Joo-Sung Kim, Yong-Keun Park, **Hyun-Seok Whang**, Jung-Hyun Park, Byoung-Chul Min, and Sug-Bong Choe, “Artifact-free optical spin-orbit torque magnetometry”, Appl. Phys. Lett. 114, 182402 (2019).

6. **Hyun-Seok Whang** and Sug-Bong Choe, “SHEM-SO”, under review.

Abstract in Korean (국문 초록)

강자성 물질은 정렬된 자화의 상태가 외부 요인에 의해 깨지지 않는 한, 반영구적으로 자기장을 가진다. 이것은 자화가 일종의 비휘발성을 가진다는 것을 의미하며, 이는 자화를 변화시킬 수 있는 적절한 방법이 갖추어진다면, 자성물질을 이용하여 저전력의 저장장치를 구현할 수 있다는 것을 의미한다. 실제로 1980 년대부터 거대 자기 저항 효과 (giant magnetoresistance: GMR)와 스핀 토크 현상 (spin torque)이 발견됨으로써, 자화가 각자 전기적으로 측정되거나, 컨트롤 될 수 있게 되었고, 이로 인해, 물질의 스핀 상태가 본격적으로 전기 소자에 응용되기 시작하였다. 주로 논리 및 메모리 소자에 응용되는 관련 분야에 대한 제반의 연구를 스핀트로닉스 (spintronics: spin electronics)라고 부른다.

스핀트로닉스는 언급하였듯이, 스핀들의 집단 현상에 깊게 관계되어 있기 때문에, 시스템에 주어진 여러 제한 조건들에 의해, 완전히 새로운 현상이 발견될 뿐만이 아니라, 그 조건을 이용함으로써, 원하는 특성을 디자인 할 수 있는 가능성까지 갖추고 있다. 여러 제한조건들 중, 간단한 3 층 구조의 강자성 박막이 놀랍도록 복잡한 스핀 동역학을 보이는 것이 알려져 있다. 강자성 물질만이 아닌, 이웃하는 층의 물질과 두께, 경계면의 조건 등에 의해 다양한 자성 특징이 관찰되고 있고, 이 논문 또한 이러한 3 층 구조에 전류가 주입되었을 때 나타나는 여러 현상을 밝히고 이용하는 데 핵심을 두고 있다.

3 층 구조 필름의 여러 흥미로운 동역학 중에서도, 자성층에 이웃한 물질층에서 일어나는 스핀 홀 효과 (spin-Hall effect: SHE)는 디자인의 용이함에 있어 뛰어난 모습을 보인다. 스핀 홀 효과의 크기와 부호는 이웃층의 물질만이 아닌 두께에 따라 바뀌기 때문에, 이웃층의 두께를 바꾸어주는 것만으로, 자성층에 스핀 홀 효과로 인해 전달되는 스핀 토크의 크기 및 부호를 마음대로 바꾸어 줄 수 있다. 이

기술은 스핀 홀 효과 조정 기술 (spin-Hall effect modulation)으로 불리며, 이 논문은 이 스핀 홀 효과 조정 기술을 이용하여 스핀 홀 효과의 크기 및 부호가 다른 영역을 만들어 준 특수한 시스템들에서 어떤 새로운 스핀 동역학이 관찰 될 수 있는지를 미소자기시뮬레이션 (micromagnetic simulation)과 이론적 분석을 통해 연구하였다.

챕터 2 는 전류로 구동되는 자구벽 (domain wall: DW)이 어떻게 스핀 홀 효과 조정 경계면에서 피닝 (pinning) 및 디피닝 (depinning) 되는 지 소개한다. 주어진 조정 경계면에서의 한쪽 방향으로 자구벽을 디피닝 시키는 방법이 소개되며, 이를 이용하여, 자구벽을 흐르는 전류의 부호를 바꾸어주는 것만으로 순차적으로 다음 조정 경계면으로 패스해나갈 수 있는 구조적인 방법을 구현함으로써, 학계의 주요 관심사인 레이스트랙 메모리의 실현에 한 걸음 더 다가간다.

챕터 3 는 본 논문의 하이라이트로써, 스핀 토크 진동자의 새로운 컨셉을 기울어진 스핀 홀 효과 조정 경계면에서의 자성 스커미온 (skyrmion)의 동역학을 이용하여 구현한 결과를 소개한다. 진동자 구조 내부에서, 스커미온은 서로 스핀 홀 효과의 부호가 반대인 스핀 홀 효과 조정 영역 사이의 경계면을 따라 돌며, 이는 미소자기시뮬레이션을 통해 확인되었다. 새로운 컨셉인 스핀 홀 효과 조정 스커미온 진동자 (spin-Hall-effect-modulation skyrmion oscillator: SHEM-SO)는 현재까지 제시되어 있는 스핀 토크 진동자들의 모든 결함을 극복할 수 있을 것으로 기대된다.

챕터 4 에서는 현재 스핀트로닉스가 새로이 역할을 할 바이오 모방 신경 공학 (neuromorphic engineering)에서 얻은 결과를 간략히 소개한다. 전류 구동 자구벽 움직임과 자기 터널 효과를 이용하여, 적분 및 발사 (integrate and fire) 기능을 구현한 뉴론 장비가 이미 제시되어 있는 자구벽 시냅스

디바이스와 합쳐져, 자구벽만으로 구현 가능한 인공 신경망 구조가 소개된다.

추가적으로, 자기 특성을 측정하거나, 새로운 장비의 디자인 룰을 제공하는 데 도움이 될 수 있는 여러 분석식들을 유도한 결과를 소개한다. 삼각 놋치 구조에서의 디피닝 전류의 식과, 임의의 자화 각도에서 스핀 궤도 토크 (spin-orbit torque)를 측정하는 데 필요한 식과, 광자기 컬 효과 (magneto optical Kerr effect: MOKE) 셋업 상에서 수직 비등방성 자기장 (perpendicular magneto anisotropy field)를 측정하는 데 필요한 식 등을 유도한 결과를 챕터 5 에서 간략히 다룬다.

본 논문에 기술되어 있는 발견들은 스핀 홀 효과 조정 시스템에 대한 최신의 이해를 제공한다. 이런 시스템들에서 설명되는 스핀 동역학은, 최신 스핀트로닉스 장비들의 기준을 한 단계 업그레이드할 뿐만이 아니라, 틀에 박힌 스핀트로닉스 소자의 디자인 룰을 타파하고, 온전히 새로운 방식의 접근을 가능케 한다는 점에서 의의를 가진다.

Acknowledgements (감사의 글)

길다면 길고 짧다면 짧은 박사 6 년의 기간 동안 쉬운 일만 있던 것도 아니었지만, 괴로운 일만 있던 것도 아니었습니다. 굴곡진 박사과정에 대한 본인의 그리고 타인의 평가는 결국 잃은 것과 얻은 것의 차이로써 흐르는 시간이 드러내 줄 것입니다. 하지만 여기서는 시대의 조각이 되어버릴 결과의 무게보다는 과정 속에서 동반자가 되어 준 주변사람들에게 시선을 돌리고자 합니다.

누구보다 먼저, 홀몸으로도 무엇 하나 부족한 점 없이 저를 지탱해 주신 어머니께 감사합니다. 어머니의 헌신을 경험하지 못했다면, 이 모든 감사가 겉치레의 메아리에 그쳤을 것입니다. 제 시작점이자 보금자리가 되어 준 어머니, 누나, 이모들과 삼촌들, 사촌 형, 누나, 동생, 조카들 모두에게 감사드립니다. 나아가, 상대하기 어려운 제 성격에도 언제나 웃음을 잃지 않아 준 연구실 선배, 동료, 후배들에게도 어수룩한 표현보다 큰 감사의 마음을 가지고 있었음을 밝힙니다. 미래의 모습으로 길잡이가 되어 주신 상준이 형, 정구 형, 승근이 형, 준이 형, 상철이 형, 덕호 형께, 현재의 고난과 행복을 동고동락한 대연이, 주성이 형, 윤석이, 용근이 형, 민호 형, 찬희, 세영이 형에게, 그리고 마지막으로 과거의 모습으로 포기하지 않고 힘내 주었으면 하는 지성이, 성협이, 준영이, 정현이, 재성이, 명회에게 모두 감사합니다. 그리고 가장 가까운 동반자로써, 누구보다 제 모습을 정확히 알고, 매일 아침 다시금 힘을 낼 수 있게 해 준 여자 친구에게도 항상 감사합니다.

그리고, 이 모든 것을 가능하게 해 주신 최석봉 교수님께도 감사의 말씀을 올립니다. 목표로서 언제나 흔들림 없는 모습으로 있어 주셨기에, 비록 턱까지 물이 차오르거나 매달릴 아귀 힘이 차마 약해질 때에는 가혹하다 생각한 적도 없지 않았지만, 결국 연구라는 황야에서 변하지 않는 나침반이

언제나 곁에 있다는 것은 감사해 마지 않을 점이였다는 것을 늘그막에라도 깨달았습니다.

이런 과분한 주변사람들 사이에서 6 년 동안 채워 온 지식은 어찌 보면 그 순간을 위한 것에 더 가깝고, 과장을 보태어 잊혀져 갈 것이라 치부한다면, 진정으로 얻은 것이라고 할만한 것은, 단순한 정보의 저장보다는 논리적인 사고력과 과학적 방법론이라고 하여도 무방할 것입니다. 이것은 이미 제게 언제 어디에서 어떤 일을 하더라도 무시할 수 없는 제 2 의 본능처럼 자리잡았습니다. 하지만 과학적 방법론으로는 설명할 수 없는 일종의 노이즈에 해당하는 무작위한 사람 간의 인연이 본인의 인생에 무엇보다 큰 영향을 주었고, 또 줄 것이라는 점 또한 부정할 수 없는 사실입니다. 큰 구조에서 동형이지만, 삶은 작은 구조의 미세한 차이에 의해 크게 뒤섞이고 들썩입니다. 그 모든 뒤섞임이 즐거운 경험은 아니겠지만, 그 뒤섞임 자체를 소중히 여기게 되면, 과학적 방법론의 거대함과 허무함 속에서 문득 길을 잃을 때라도 다시금 제자리로 돌아올 수 있다고 믿습니다. 이 감사의 글 또한 결국 스쳐 지나간 수백 수천의 글들과 별다를 바 없겠지만, 적당한 때를 맞아 풍화와 침적으로 제 모습을 조각해 준 수 많은 인연들에게,

감사합니다.

2019.07.08. 황현석 씀.